6 Injector

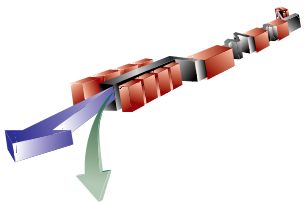

TECHNICAL SYNOPSIS

The injector for the LCLS is required to produce a single 150-MeV bunch of charge 1.0 nC and 100 A peak current at a repetition rate of 120 Hz with a normalized rms transverse emittance of 1.0 μm. The required emittance is about a factor of 2 lower than has been achieved to date. The design employs a solenoidal field near the cathode of a specially designed rf photocathode gun that allows the initial emittance growth due to space charge to be almost completely compensated by the end of the booster linac. Following the booster linac, the geometric emittance simply damps linearly with energy. PARMELA simulations show that this design will produce the desired normalized emittance.

In addition to low emittance, there are two additional electron-beam requirements that pose a challenge: the timing and intensity jitters must have an rms value of ≤0.9 ps and ≤2% respectively. For an rf photoinjector, these parameters are determined principally by the laser system. Commercial laser oscillators are available with a timing stability of 0.5 ps. The laser system described here uses feedback loops to maintain this stability in the amplification and pulse shaping stages. The desired laser-pulse energy tolerance is achieved by stabilizing the pumping laser for the amplifiers and by operating the second amplifier in saturation. RF systems with a phase stability of 0.5 ps are already routine for the SLAC linac.

Although additional R&D is in progress to ensure the performance of the photoinjector as planned, confidence in the present design is based on the performance of existing systems and projected improvement based on multi-particle code simulations. Simulations using these same codes match the measured performance of rf photoinjectors operating near the emittance level desired. Laser systems have been employed in high energy physics experiments with timing stability—with respect to the accelerated electron beam—that is close to the value required.

The injector is divided geographically between the electron source—consisting of an rf gun and laser system—the booster linac, and the Matching Section. However, to produce the minimal transverse emittance at high energy, the photoinjector must be treated as one unit.

6.1 Introduction

Unlike light sources based on storage rings for which the beam properties of the stored beam due to synchrotron radiation are almost entirely decoupled from the properties of the injector beam, the performance of a linac-based Free Electron Laser (FEL) is directly dependent on the quality of the electron drive beam as produced by the injector and preserved by the main linac. As discussed in **Chapter 4**, *FEL Physics*, the optimum phase-space matching between the FEL electrons and photons is achieved if the electron beam emittance is $<\lambda/4\pi$, where λ is the wavelength of the FEL radiation. A somewhat higher emittance can be accommodated by increasing the length of the undulator. The proposed Linac Coherent Light Source (LCLS) is an X-ray FEL that will use the final third of the SLAC 3-km linac for the electron drive beam. The performance of the LCLS in the 1.5-Å regime is predicated on the availability of a 1-nC, 100-A beam at the 150-MeV point with normalized rms transverse emittance of 1 μm. With this emittance, an undulator length of ~100 m is required. An experimental program is underway at the Gun Test Facility (GTF) at SLAC to demonstrate a high-brightness beam meeting the LCLS requirements [1]. The GTF experiment uses a 1.6-cell S-band rf gun developed jointly with BNL and UCLA [2]. The gun exit is surrounded by a solenoid. After a short drift there is a standard SLAC 3-m accelerating section. At BNL using a similar configuration, a transverse normalized rms emittance of 2.4 μm for a 0.9 nC pulse with 10-ps FWHM Gaussian pulse length has been measured [3]. Simulations indicate that a factor of 2 decrease in emittance is expected if the temporal pulse shape is uniform rather than Gaussian. Unfortunately, all experiments to date have used the natural temporal pulse shape of the source laser, which generally approximates a Gaussian distribution.

Earlier simulation studies using the multi-particle code PARMELA predicted a transverse normalized emittance of 1 μm—thermal emittance not included—for the LCLS photoinjector if a uniform (or even a truncated Gaussian) temporal charge distribution were used [4] as well as a uniform transverse distribution. While this result technically meets the LCLS requirements, it leaves no headroom for errors or practical difficulties. Consequently, simulation studies have continued with the goal of finding a photoinjector design for the LCLS that predicts a transverse emittance of no more than 0.8 μm with the thermal emittance included.

Following the introduction and survey of experimental results, the chapter is divided into 4 major sections. The rf photocathode gun is described in some detail although a complete conceptual design does not yet exist. This is followed by a thorough explication of the Ti:sapphire drive laser system and then the proposed injector layout with instrumentation indicated. The final section is devoted to simulations.

6.1.1 Beam Requirements

The LCLS injector is required to produce a single bunch with nominal charge, Q, of 1 nC at a repetition rate of 120 Hz. After acceleration to 150 MeV, the bunch is required to have a peak current of at least 100 A and an integrated normalized rms emittance of $\leq$1 μm. These parameters

correspond to those predicted for an optimized S-band photoinjector using emittance compensation and assuming an electron bunch with initial uniform spatial and temporal charge distributions with σ_r and σ_z of 0.71 mm rms and 2.9 ps rms respectively. The photoinjector is actually designed to allow optimized performance with bunch charge as low as 0.2 nC. Given an optimized injector design for 1 nC, as the charge is lowered the emittance will remain optimized if the charge density is held constant by scaling each dimension of the bunch as $Q^{1/3}$. Thus bunches with σ_z as short as 2 ps may be needed. Then, if the effects of thermal emittance are ignored, the optimized integrated emittance is expected to scale as $Q^{2/3}$ [5].

A low energy spread at 150 MeV is also required. An acceptable value of $\sigma_\gamma / \gamma_o \le 0.1\%$ will be achieved for the integrated bunch by adjusting rf phases in the booster linac. An electron bunch can be analyzed in terms of axial slices. Unless otherwise specified, the thickness of a slice is some minor fraction of the total longitudinal width of the bunch. While the slice energy spread is important, it cannot be readily adjusted. A value of $\sigma_\gamma^{slice} / \gamma_o \le 0.02\%$ at 150 MeV is desired.

In addition to low emittance and energy spread, there are two additional challenging requirements that are derived from the sensitivity of the current and energy jitters in the undulator to the charge and timing jitters at the gun. The first of these challenges concerns charge jitter at the gun. Simulations indicate that the rms peak current jitter in the undulator—where rms values are measured over a few seconds with the LCLS operating at 120 Hz—will be 12% for an rms charge jitter at the gun of 6%. (See **Table 7.4**.) However, when all sources of current jitter are taken into account, the rms charge jitter at the gun must be reduced to the order of about 2% to maintain the 12% rms peak current jitter at the undulator. (See **Table 7.5**.) Since the goal is to keep the rms peak current jitter in the undulator under 12%, a criterion of ≤2% has been adopted for the rms charge jitter for the LCLS photoinjector gun. **Section 6.4**, *Laser System*, describes how this tolerance will be achieved.

The second challenge concerns the timing jitter of the electron bunch with respect to the rf driving the gun and linac. The timing jitter affects both the peak current and energy in the undulator. To keep the rms peak current jitter in the undulator below 12%, the rms timing jitter need only be less than 4.0 ps. However, the rms timing jitter must be less than 1.4 ps to maintain the rms energy jitter in the undulator below the desired 0.1% (**Table 7.4**). But again, when the various sources of energy jitter are considered together, the rms timing jitter at the gun must be reduced to the order of 0.9 ps (**Table 7.5**). In **Section 6.4**, *Laser System*, it is shown that a value of ≤0.5 ps for the rms timing jitter of the electron bunch with respect to the rf driving the gun and linac should be achievable. Since accomplishing this goal will slightly relieve the charge jitter criterion at the gun, this lower value of timing jitter has been adopted as the criterion for the injector laser system.

These beam requirements are summarized in **Table 6.1** below.

Table 6.1 Summary of Beam Requirements at End of L0.

Parameter	Value
Charge per e^- bunch, Q_0	1 nC
Repetition Rate	120 Hz
Energy	150 MeV
Peak current	100 A
Normalized projected transverse emittance, $\varepsilon_{n,rms}$	≤1μm
Integrated energy spread, σ_γ/γ_0	≤0.1% rms
Slice energy spread, $\sigma_\gamma^{slice}/\gamma_0$	≤0.02% rms
Timing jitter with respect to rf, Δt_0	≤0.9 ps rms
Charge jitter, $\Delta Q/Q_0$	≤2.0% rms
Bunch length jitter, $\Delta l_0/l_0$	≤5% rms

6.1.2 Emittance Compensation

The theory of linear emittance compensation in a high brightness rf photoinjector is well established [6,7]. It has been shown that the optimization of an rf photo-injector corresponds to accelerating and propagating the beam through the device as close as possible to two beam equilibria: a laminar Brillouin flow in drifts, and the so-called Invariant Envelope (IE) in accelerating sections. The IE is a generalization of Brillouin flow for an accelerated beam when rf focusing effects and spot-size adiabatic damping are taken into account. In the space-charge dominated regime, i.e., when the space-charge collective force is largely dominant over the emittance pressure, the bunch behaves as a laminar flow and can be represented in a simple model as a set of slices, each one described by an envelope equation that includes the local slice space-charge field. Mismatches between the space-charge correlated forces and the external focusing gradient produce slice envelope oscillations whose plasma frequencies can be computed from the model. The result is that plasma frequencies are independent of the slice currents to first order, i. e., all the slices have the same plasma frequency although the slice current affects the amplitude of each oscillation. This frequency independence results in reversible normalized emittance oscillations: a minimum emittance is correlated with an integral number of plasma oscillations for which the slices are periodically aligned in transverse phase space, and accelerating the beam through the IE damps these oscillations as the square root of the beam

energy. Provided the oscillations are properly tuned, the normalized emittance reduces to a steady state minimum at the injector exit.

As a consequence of such a theory, the definition of the injector region has to be extended up to an energy high enough to exceed the laminar regime. The beam then enters the so-called emittance-dominated regime, where trajectory crossovers dominate over space-charge oscillations, and, in an ideal accelerator, the total normalized emittance remains constant.

The laminar regime extends up to an energy, γ, given by [7]:

$$\gamma = \sqrt{\frac{2}{3}} \frac{\hat{I}}{I_0 \varepsilon_{th} \gamma'} \tag{6.1}$$

where ε_{th} is the thermal emittance, I_o=17 kA is the Alfvén current, $\hat{I}$ the peak current. The derivative of γ with respect to z is given by $\gamma' = eE_{acc}/m_e c^2$, where E_{acc} is the accelerating field. With the expected LCLS parameters: $\hat{I}$=100 A, E_{acc}=25 MV/m and an estimated ε_{th} of 0.3 μm for a Cu cathode with UV excitation [8], the transition occurs at about 150 MeV. For this reason the emittance compensation process of the LCLS injector has to be optimized up to the exit of the booster linac, before injecting the beam in the main linac.

It follows from the discussion above that the basic point in the design of a photoinjector is to match properly the beam from the gun to the booster. This is done for a space-charge dominated beam falling within the paraxial limit if the following IE conditions [7] are met: first that the derivative, σ', of the rms transverse spot size,)σ, with respect to the independent variable z is such that

$$\sigma' = 0, \tag{6.2}$$

implying a laminar waist governs at the booster entrance; and second that

$$\gamma' = \frac{2}{\sigma} \sqrt{\frac{\hat{I}}{2 I_0 \gamma}}, \tag{6.3}$$

which gives the matched accelerating field for a traveling wave (TW) structure.

To optimize the photoinjector design, the semi-analytical code HOMDYN [9] was chosen to investigate the booster matching condition, taking advantage of the fast running capability of the code to explore a wide range of parameters. The next section describes how HOMDYN was used to find the optimal conceptual design for the injector, while the more tedious but also more detailed physical optimization using the tracking code PARMELA is described in **Section 6.6**, *PARMELA Simulations*.

6.1.3 Design Principles

The discussion here assumes the 1.6-cell S-band rf gun developed jointly with BNL and UCLA [2] surrounded by a solenoid just after the gun exit. After a drift, the gun is followed by two standard SLAC 3-m traveling wave (TW) accelerating sections. As discussed in reference

[10], for a 1-nC uniform-charge distribution and a 10-ps long bunch with 1-mm hard-edge radius, good emittance performance and high peak current at the exit of the gun can be obtained with a peak field on the cathode of about 140 MV/m, an injection phase (with respect to the rf zero crossing) on the order of 35°, and a moderate solenoid field strength of about 3.0 kG. Earlier design studies for the LCLS injector made use of a low-gradient booster as was then the standard [4]. In the following analysis, these parameters, which in this context will be called the *standard* or *old working point*, are taken as the starting condition for a new parameter-space search.

When observing envelope and emittance behavior while scanning the gun solenoid field strength using HOMDYN, an interesting feature can be seen that appears to be a very effective *new working point* for a split (gun separate from booster) rf photoinjector [11]. By increasing the solenoid strength, the emittance evolution shows a double minimum behavior in the drift region following the gun. For a unique value of the solenoid strength (3.1 kG in this case) the envelope waist occurs where the emittance has its relative maximum (z≈1.5 m in this case) as shown by the red (bold) lines in **Figs. 6.1 and 6.2**. The solenoid value that produces this unique coincidence of waist and emittance relative maximum is a key constituent of the new working point.

The performance using the new working point relies on this feature of the emittance oscillation. If the booster entrance is located at z ≈ 1.5 m, where the beam laminar waist occurs, and if simultaneously the other IE matching condition is satisfied, i.e., **Eq. (6-3)**, the second emittance minimum can be shifted to higher energy and frozen at a lower level, taking advantage of the additional emittance compensation occurring in the booster.

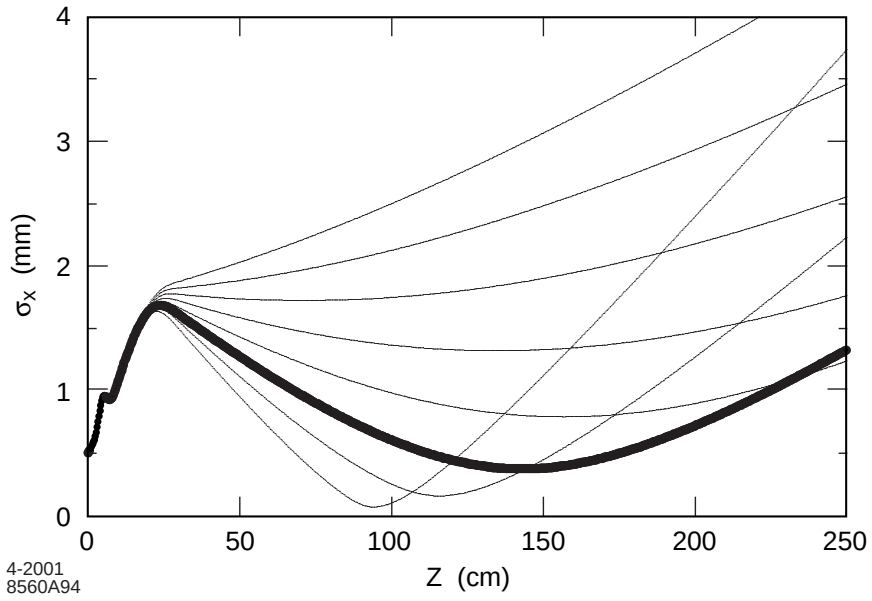

Figure 6.1 Beam envelope versus z. Each curve is for a different solenoid strength, i.e., values between 0.26 and 0.33 T in equal increments.

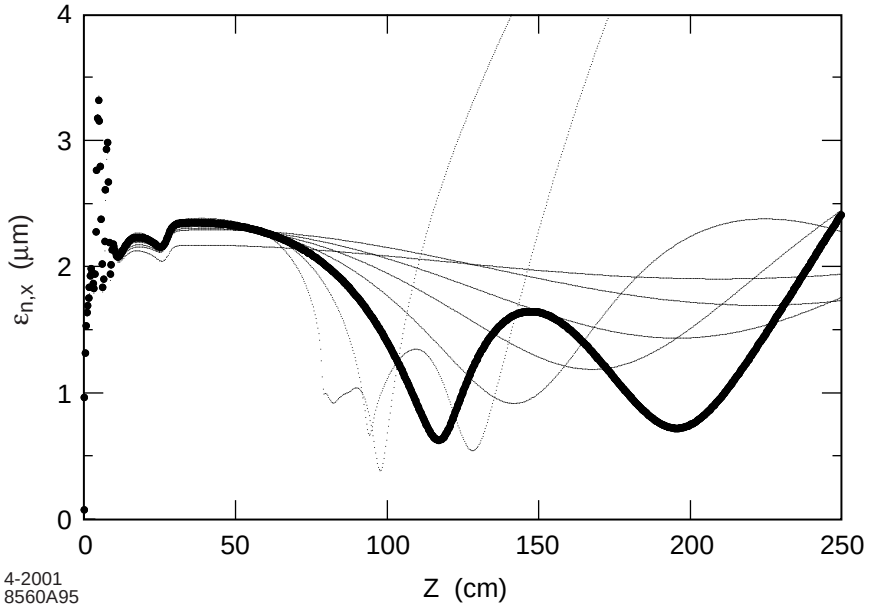

Figure 6.2 Beam emittance versus z. Each curve is for a different solenoid strength, i.e., values between 0.26 and 0.33 T in equal increments.

Since the minimum rms spot size in **Figure 6.1** for the conditions of the new working point is σ=0.41 mm, the current averaged over the slices is 96 A, and the average slice energy is 6.4 MeV, the matched accelerating gradient of the traveling wave (TW) booster is required to be 35 MV/m. Two SLAC 3-m accelerating structures are required to drive the beam out of the space charge dominated regime, resulting in an energy of 216 MeV in an 8-m long injector line (assuming a 0.5-m long drift in between the two structures and not including the gun structure upstream of the cathode). As expected, the second emittance minimum, which is 0.5 μm, now occurs downstream of the booster structures, at z=10 m. (This location will be taken as a reference position to quote emittance at the injector exit).

Despite the good emittance resulting from this design, the necessary gradient to match the beam to the booster exceeds the limit of reliable performance by available SLAC 3-m structures. One solution is to shift the solenoid location downstream and set the solenoid strength so as to recover the new working point conditions. By doing so the resulting spot size at the waist is bigger and thus, from **Eq. (6.3)**, a lower matched gradient is required.

A lower gradient solution can also be achieved by increasing the focusing properties of the booster [12]. This can be done by means of standing wave (SW) structures or equivalently by a long solenoid around the first TW structure [11]. The second solution is chosen for the LCLS design to simplify the rf system. Setting the desired accelerating field of the TW sections to 26 MV/m and scanning the long solenoid strength, a very good working point is indicated for a longitudinal field of B_z=800 G. A beam dynamics simulation using HOMDYN indicates a very low emittance value, of 0.2 μm (thermal emittance not included) at 160 MeV as shown in **Figure 6.3**, while at the same time the other relevant LCLS requirements are very nearly fulfilled. For example, the peak current of 95 A is only slightly below the desired value. The energy spread

can be minimized by injection into the booster off-crest. However, in this case the optimized phase of 12° (relative to the crest) results in a residual rms energy spread at the exit of the booster of 0.25%, which is 2.5 times the required value. In any case the final optimization must be done with a multi-particle tracking code.

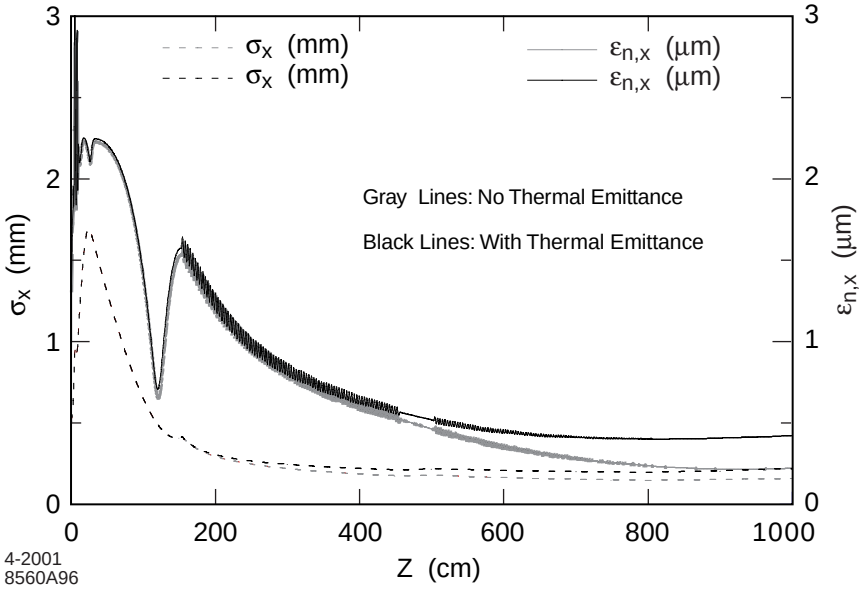

Figure 6.3 Beam envelope and emittance along the injector beamline, without thermal emittance (red/lower lines) and with thermal emittance (black/upper lines).

In this design the total emittance is limited by the thermal emittance contribution. **Figure 6.3** also shows the emittance evolution as computed by including a value of ε_{th}=0.3 μm, where the strength of the long solenoid has been reduced to B_z=700 G to recover an optimized design. The resulting total emittance is 0.4 μm.

6.2 Summary of Experimental Results

The design of the LCLS rf photocathode gun is based on the 1.6-cell low-emittance S-band rf photocathode gun (herein called the "prototype gun") that was designed by the BNL/SLAC/UCLA rf gun collaboration for x-ray FEL applications [2]. There are at least seven prototype guns in operation including guns at ANL, BNL, LLNL, SLAC, UCLA and the University of Tokyo. These guns all use the 1.6-cell symmetrized S-band design with several variations of mechanical contact and tuning of the cathode plate as well as modifications in the cooling capability due to different cooling channel locations. The design of the gun requires the emittance compensating solenoid to be located very close to the cathode. Several of the guns use a second solenoid behind the cathode to null the magnetic field at the cathode plane, while most use a steel flux return for the single solenoid to limit the field at the cathode to less than 5 G. Despite these variations, all of the guns are electrically identical and are all theoretically capable of producing essentially identical beams, assuming identical drive laser pulses are used. All the guns use metal cathodes, either Cu or Mg. Several of the guns have been operated at peak electric

fields exceeding 120 MV/m for limited periods, but to date no gun with a Mg insert has consistently operated at fields higher than 110 MV/m.

6.2.1 Quantum Efficiency

While a metal cathode assures the ability to utilize the high field necessary to produce low-emittance beams, it also necessarily results in a cathode with relatively low quantum efficiency[a] since the metal reflects the vast majority of the incident photons. Depending on the cathode history, the QE for a Cu cathode can vary from a low of roughly 10^{-6} to a high of nearly 10^{-4}. Recent measurements at UCLA on a clean-single crystal Cu (100) surface (chosen to minimize grain boundary scattering) resulted in a QE of 4.6×10^{-5} with 90 MV/m peak field at the cathode and a 45° emission phase (measured with respect to the zero field crossing) [13]. The QE for an identical cathode at SLAC was measured to be $3.6\text{x}10^{-5}$ with an applied field of 100 MV/m at a 38° emission phase [14]. A polycrystalline Cu cathode at SLAC with 100 MV/m peak field resulted in a QE of 6.1×10^{-5} at 50° emission phase as shown in **Figure 6.4**. Scaling these results to the LCLS operating parameters of 140 MV/m and 32° phase, one expects a QE of greater than 7×10^{-5}. For the purposes of this report, a conservative value of QE of 1×10^{-5} is assumed to be readily achievable.

If the cathode is not installed in a clean manner, surface contaminants can lead to significant reduction in the QE and also to spatial variation in QE. Such variations have been measured at SLAC with a cathode that was not installed in a sufficiently controlled environment [1]. **Figure 6.5 (A)** shows the measured QE as a function of position across this cathode. Fluctuations greater than 50% were measured by scanning a laser beam 1 mm x 0.3 mm across the cathode at grazing incidence. The average QE was $<1\times10^{-5}$. Subsequently the laser intensity was increased and scanned across the cathode again under the explosive emission regime [15]. There was a short term decrease in the QE spatial variation and significant improvement in the average QE as shown in **Figure 6.5 (B),** but at the expense of a significant increase in the micro-roughening of the cathode surface and the emitted dark current. The improvement in QE was only short lived (weeks) and eventually led to even larger spatial variations than initially measured. Subsequent cathodes installed in more stringently-controlled environments exhibited significantly higher QEs as shown in **Figure 6.4** and less spatial variation in the QE as well. Only 10% rms fluctuation in the QE over a 2.5 X 2.5 mm area was measured at the GTF [14] after installing the cathode under a nitrogen environment. Thus for the LCLS gun, a load-lock will be implemented for installing cathodes to insure completely reproducible and controlled environments so that consistently high and relatively uniform QEs can be achieved.

[a] Quantum efficiency (QE) is herein defined as the number of electrons that escape to vacuum from the photocathode surface per incident (as opposed to absorbed) photon. A single photon wavelength is always assumed.

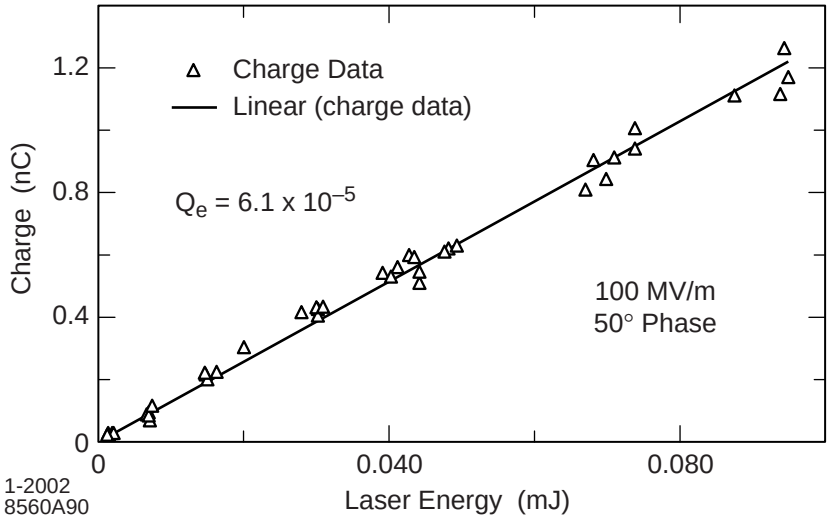

Figure 6.4 The measured charge extracted from a Cu photocathode as a function of laser energy with 100 MV/m peak rf field and 50° laser injection phase.

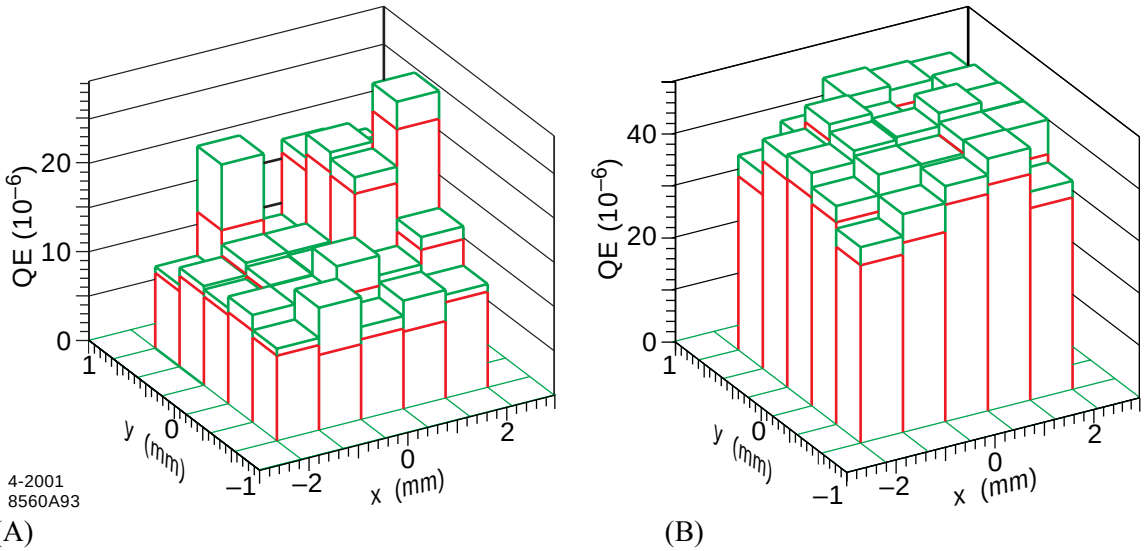

Figure 6.5 The measured quantum efficiency is plotted for a Cu cathode both before (A) and after (B) laser cleaning. The error in the QE values is indicated by the green slices at the top of each QE column.

6.2.2 Transverse Emittance Measurements

The history of the lowest emittance measurements for 1 nC of charge is summarized **Figure 6.6**. The lowest emittances to date have been achieved with solenoidal emittance compensated photoinjectors with the lowest measured values near 2 μm as described below. These measurements are consistent with the predictions of tracking codes like PARMELA if the physical parameters of the experiments are taken into account. PARMELA simulations also indicate that emittances on the order of 1 μm should be achievable if the Gaussian temporal

charge distribution used in these experiments were replaced with one that is uniform, i.e., flattop. In addition, simulations for more recent photoinjector designs (see for example **Section 6.6.** *PARMELA Simulations*), now predict an emittance significantly less than 1 μm.

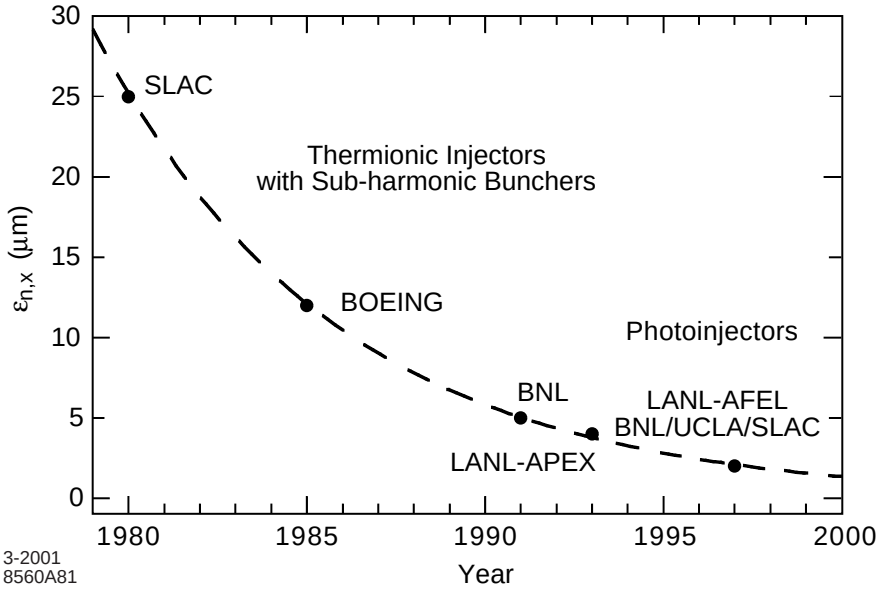

Figure 6.6 Normalized rms transverse emittance measured by the leading thermoionic (SLAC, BOEING) and rf photocathode injectors [16]. All data are for bunched beams with approximately 1 nC of charge.

In the 1-nC regime, the lowest reported projected, normalized, rms emittance for an S-band gun is 2.4 μm measured at BNL [3] using a two-screen emittance measurement technique with 0.9 nC of charge. The emittance was measured using an approximately flat top transverse laser (clipped Gaussian) distribution and a 15-ps FWHM approximately Gaussian temporal distribution. However, the electron beam bunch length downstream of the booster accelerator was closer to 4 ps FWHM, which was attributed to rf compression in the gun. The beam was also measured using a quadrupole scan technique, which resulted in an emittance of 3.2 μm with 0.8 nC of charge. The different results in the two measurement techniques were attributed to background subtraction errors in the quadrupole scan technique. A constant background obtained with a closed iris was used for background subtraction, while the real background varied with the electron beam image size due to image intensity changes during the quad scan. Since the beam size and, therefore, the intensity did not change during the two-screen measurement, the error is assumed to be less.

Temporal slice emittance measurements were also achieved on the same machine with roughly 1-ps resolution. By phasing the last booster accelerator section, a linear energy chirp (energy vs. time) on the beam was created and then spatially filtered in a dispersive section allowing only a narrow time slice through the slit. The resolution was limited by the minimum achievable electron beam size primarily due to the intrinsic uncorrelated energy spread in the beam and the jitter in the rf system. A two-screen emittance measurement setup was located

downstream of the spatial filter. This type of slice measurement necessarily has some effect on the electron beam distribution since the linac phase is varied from the nominal operating parameters. BNL reports a slice emittance of 1.2 μm for a 1-ps slice with 0.08 nC and a full beam charge of 0.9 nC with identical beam parameters as reported above [3]. The reported slice contains less than 10% of the total charge but covers roughly 25% of the electron beam pulse length.

At LANL, a 1.3-GHz integrated photoinjector (no drift space between gun and booster accelerator) has produced the lowest reported projected emittance to date from an L-band gun: 2.5 μm with 1.1 nC of charge [17]. The laser beam used had a clipped Gaussian transverse distribution (approximately 15% variation across the beam) with 5.2-mm diameter and a 17-ps FWHM Gaussian temporal distribution. The electron beam bunch length was measured to be 15 ps FWHM using a streak camera. The measurements were performed with a 26 MV/m peak field on the cathode and an emission phase of 19°. This measurement used a streak camera with a 20 μm slit to acquire time resolved images of quadrupole scans. The beam size was roughly 0.5 mm rms, and therefore this technique necessarily resulted in effectively analyzing single lines of the electron beam digitized image instead of full projections because of the presence of the streak camera input slit.

The streak camera used to acquire data for the projected emittance at LANL was also used for collecting slice emittance data. The slice emittance measurements were accomplished with approximately 7-ps resolution, which was limited by the streak camera. A more detailed description of the streak camera enhanced quadrupole scan technique is described in **Section 6.5.3**, *Slice Emittance*. With identical beam parameters as described above, the minimum measured slice emittance was 1.8 μm for a 4-ps slice in the center of the bunch with approximately 0.3 nC of charge. This slice contains almost 23% of the charge and also nearly 25% of the electron beam bunch length.

Measurements at lower charge, but close to the LCLS design current of 100 A, have been made recently at the SLAC Gun Test Facility (GTF). Several measurements at the 200 pC level with a 2 ps FWHM temporal Gaussian laser beam resulted in an emittance of 1.5 μm in good agreement with PARMELA simulations [14]. These results indicate that emittances of approximately 1 μm can be experimentally achieved at the 100 A level. Additional measurements are being made at the GTF with temporally flat laser profiles at the 1 nC level.

As indicated in **Section 6.1**, *Introduction*, and earlier in this section, simulations show that the primary reason that emittances of 1 μm have not yet been achieved is because no experiment to date has been conducted using a temporally flat top laser pulse to produce a temporally flat top electron bunch. While a measurement with a temporally flat top laser pulse is planned for the GTF in the near future, the degree of flatness that can actually be achieved is at present not well known. A simulation study with PARMELA is underway to determine the effect of a modest modulation (on the order of 20%) would have on the emittance. The simulations also assume an azimuthally and radially independent electron beam, which is difficult to achieve experimentally. In fact the real beam depends on the convolution of the laser profile and the photocathode

response. This can lead to significant variation in the space charge forces that cannot be properly compensated with solenoidal emittance compensation. A simulation study of the effect on the emittance of a spatially non-uniform but axially symmetric modulation of the charge distribution is also in progress.

All emittance experiments also suffer from shot to shot fluctuations and imperfect background subtraction, issues that are addressed for the LCLS design primarily in **Section 6.4**, *Laser System*.

In summary, although the emittance required for the LCLS has not yet been demonstrated with an rf photoinjector for a 1-nC beam, the experimental results are consistent with PARMELA simulations. PARMELA simulations also predict that if temporal as well as transverse pulse shaping is used, the LCLS emittance values should be achievable.

6.2.2 Thermal Emittance

One concern in the production of low emittance beams is the thermal emittance of the beam due to its excess energy as it leaves the cathode. The projected and slice emittances must be greater than or equal to the thermal emittance. The ideal method of determining ε_{th} is to measure the angle-resolved energy distribution for photoelectrons emitted from the cathode. Unfortunately no such measurement has been made for a Cu cathode to date. However, the emittance exiting the gun at very low charge levels where space charge is not significant has been conducted at BNL [18]. The beam size exiting the gun is measured as a function of the solenoidal focusing strength and the emittance is then fit to the measured data. The normalized rms thermal emittance has been measured to be 0.6 μm for a 2-mm diameter Cu cathode. The emittance contribution due to the finite pulse length of the electron beam has been estimated to be less than 5%.

An alternate but indirect method of measuring ε_{th} has been suggested [19] and conducted at SLAC. For small changes in the work function of a metal, the quantum efficiency, Q_e, can be written as

$$Q_e \approx Q_{e0} e^{\frac{\Delta\Phi}{kT_e}}, \qquad \textbf{(6.4)}$$

where $\Delta\Phi$ is the change in the work function, and T_e is the effective temperature of the cathode, and Q_{e0} is the QE before the change. The change in the work function due to the Schottky effect is given by

$$\Delta\Phi = \sqrt{\frac{e^3 E_p \sin\Theta}{4\pi\varepsilon_0}}, \qquad \textbf{(6.5)}$$

where E_p is the peak applied field and Θ is the emission phase. The Schottky effect can be thought of as altering the work function of the cathode material. Using **Eqs. (6-4** and **-5)**, a value of T_e can be derived from the measured slope of $ln(QE)$ versus $(E_p sin(\theta))^{1/2}$. Then the corresponding value of the thermal emittance can be calculated from T_e using the well-known relationship for uniform emission from a thermionic cathode of radius r_c:

$$\varepsilon_{n,rms,th} = \frac{r_c}{2}\sqrt{\frac{kT_e}{m_o c^2}} \,. \qquad \textbf{(6.6)}$$

Using the data shown in **Figure 6.7**, the effective temperature is estimated to be 0.14 eV resulting in a normalized, rms, thermal emittance of 0.3 μm for a 2-mm diameter cathode.

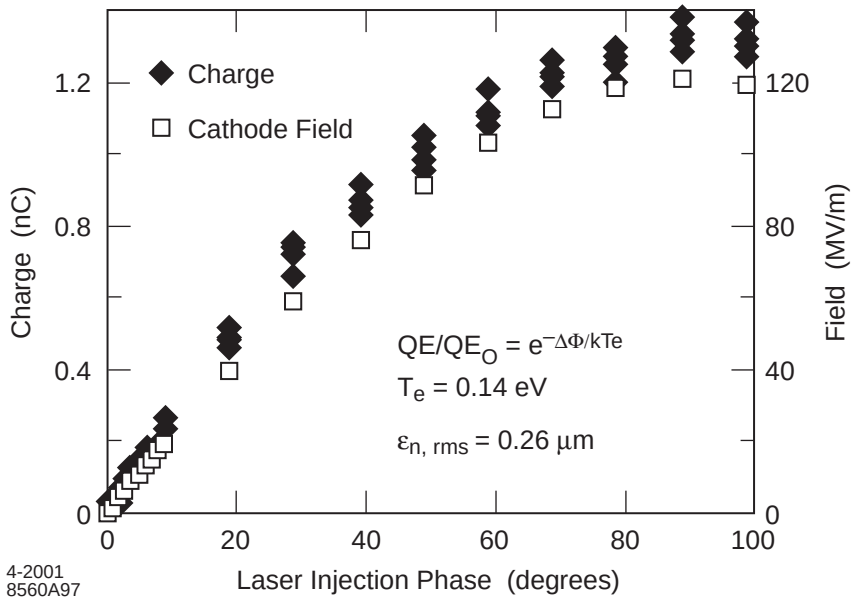

Figure 6.7 The measured charge extracted from a Cu photocathode with ≈190 μJ of laser energy and the corresponding rf field at the cathode are plotted as a function of injection phase.

6.2.3 Longitudinal Emittance

A significantly larger amount of work has been spent on measuring the transverse emittance as opposed to the longitudinal emittance. While both of the low emittance experiments at 1 nC described above reported the electron beam pulse length, neither reported the energy spread. The BNL experiment, which utilized an energy chirp by intentionally misphasing a linac section, necessarily modified the longitudinal emittance of the beam, making simultaneous transverse and longitudinal emittance measurements under nominal operating parameters impossible. The LANL experiment utilizes an integrated photoinjector so that one can not individually optimize the phase of the gun and linac to simultaneously optimize the transverse and longitudinal emittances.

Work has begun on the prototype gun to systematically measure the longitudinal emittance. Preliminary results for a low charge beam of 0.15 nC give 6.4 keV for the uncorrelated, rms energy spread out of the gun. A detailed study of the uncorrelated longitudinal emittance of a 144-MHz rf photoinjector indicates that below the space charge limit, the uncorrelated longitudinal emittance and energy spread vary linearly with the surface charge density at the cathode [20]. Using this study's parameterization, the prototype gun experimental surface charge density would give 4 keV, 40% lower than the observed 6.4 keV. Extrapolating to the LCLS charge of 1 nC, the low frequency gun study would predict 22 keV for the uncorrelated rms energy spread out of the LCLS gun. The PARMELA simulation of the LCLS gun at 140

MV/m gives 8 keV. It is clear that further effort is needed to refine and understand these differences, however they are all close to the desired specification given in **Table 6.1**.

6.3 RF Photocathode Gun

The parameters for the LCLS rf photoinjector gun are listed in **Table 6.2** below.

Table 6.2 LCLS RF Photoinjector Gun Parameters.

Parameter	Value
Cathode material	Cu (or possibly Mg)
Usable diameter of cathode	12 mm
Quantum efficiency	$>10^{-5}$ at 263 nm
Nominal peak rf field	140 MV/m
Beam energy at gun exit[a]	~7.1 MeV
Energy spread (uncorrelated) at gun exit	<0.2% rms
rf frequency	2856 MHz
Bunch repetition rate	120 Hz
rf pulse duration	~3 μsec
rf peak power for 140 MV/m	14 MW
Number of cells	1.6
Length of gun	0.168 m

a The beam energy is quoted for 140 MV/m peak field and emission phase of 32° with respect to the rf zero crossing.

6.3.1 Gun Description

The LCLS gun design is anticipated to be a variation of the BNL/SLAC/UCLA 1.6-cell S-band rf photocathode gun [2], herein called the "prototype gun." The principal differences are the addition of a vacuum load-lock to better ensure cathode performance and improved cooling to allow operation at 120 Hz. In addition, the rf power for the LCLS gun will utilize a dual feed to minimize field asymmetries. Each of these features will be discussed in more detail later. Unless specifically indicated otherwise, the gun discussed below is the prototype gun.

The 1.6-cell rf prototype gun design is based on the earlier 1.5-cell gun developed at BNL [21]. To minimize emittance growth due to the E_z component of the TM_{110} mode, the field amplitude in the gun was symmetrized. The original BNL zero-mode-suppressed side-coupling was replaced. The rf power for the prototype gun is symmetrically coupled into the full cell only, which does not suppress the zero mode. However, if the beam is extracted after several fill times of the zero mode, then the fields in the gun will be sufficiently close to the steady-state condition that the zero mode will have decayed to an insignificant level.

Since there is no direct rf coupling from the waveguide to the half cell, the cell-to-cell coupling was improved by increasing the iris size, which also increased the mode separation between the zero- and π–modes. To provide more rf focusing and decrease the peak field on the cell-to-cell iris, the half-cell length was slightly increased.

A cross section of the rf prototype gun is shown in **Figure 6.8**. The photocathode is located in the geometric center of the end plate of the half-cell. The end plate is removable to facilitate installation of cathode material other than Cu by implantation or by using an insert. As with the original BNL gun, the laser beam can be brought to the cathode either along the axis of the gun or at a grazing incidence through the 72° side port.

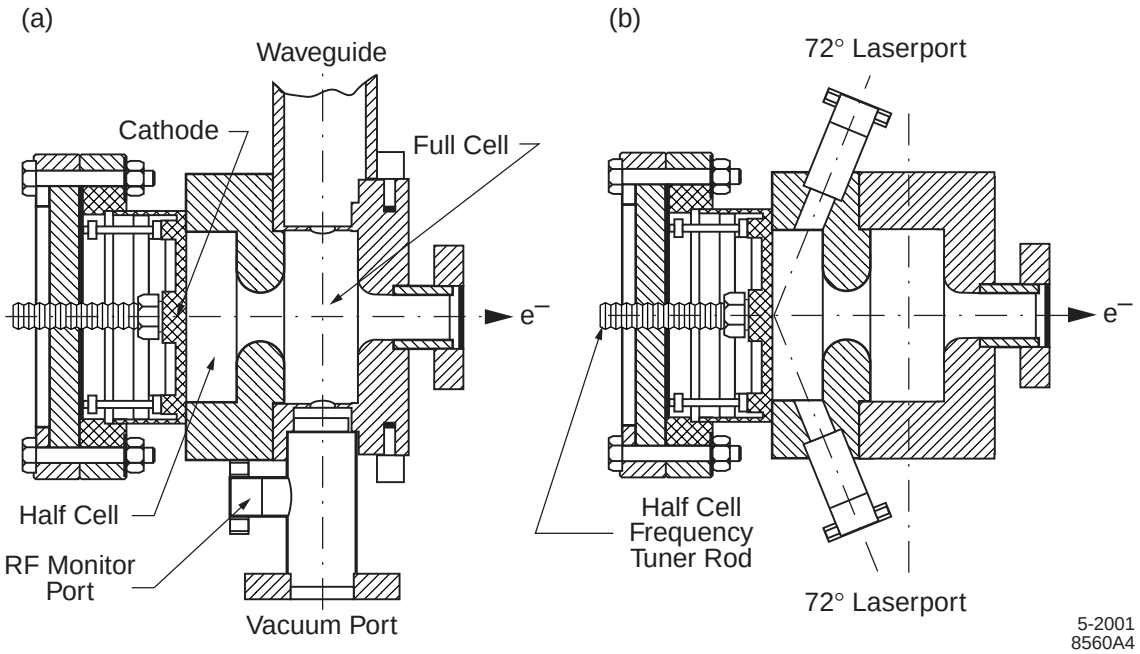

Figure 6.8 Cross section of rf prototype gun. (a) azimuthal orientation showing rf coupler and vacuum port; (b) orientation showing the off-axis laserports.

Electric field maps for the prototype gun were obtained with SUPERFISH. The π-mode fields are shown in **Figure 6.9**.

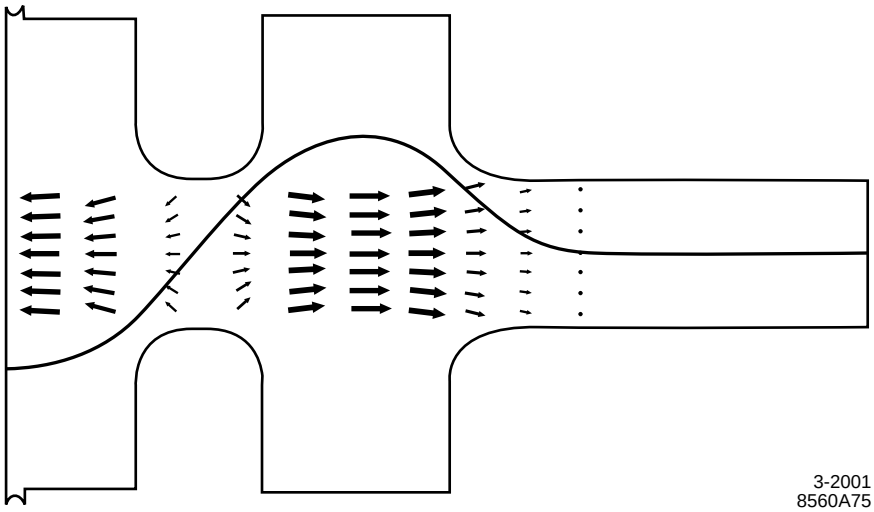

Figure 6.9 Field lines in the rf gun for π-mode obtained with SUPERFISH.

6.3.2 Field Strength and Cell Balance

Because of the deleterious effects of space charge on the beam emittance, it is important to accelerate the beam as rapidly as possible within the gun itself. Simulations indicate that the transverse emittance decreases as the field increases until about 140 MV/m on the cathode surface, at which point a local minimum in the emittance versus solenoidal and cathode field strengths has been observed using PARMELA. See **Figure 6.10**.

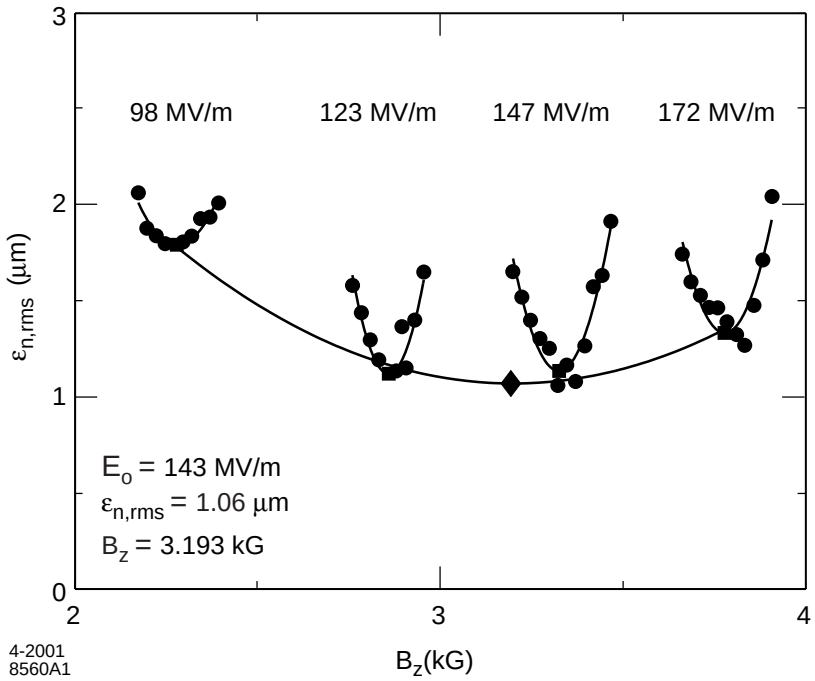

Figure 6.10 Emittance versus cathode field strength and peak solenoidal magnetic field.

Prototype guns have been operated for limited periods with fields up to 140 MV/m. However, as the field is increased above 100 MV/m, not only does the dark current typically increase rather dramatically (quickly exceeding the photocurrent), but the frequency and intensity of rf breakdowns also increases. RF breakdowns tend to leave pits in the cathode surface that lead to nonuniform emission. At the GTF, using a Cu cathode, 120 MV/m has been the typical operating field.

PARMELA simulations (See **Section 6.6.4**, *Sensitivity Study*) indicate the ratio of the field in the full cell to half cell should be close to unity. Unbalanced fields can lead to large correlated energy spreads exiting the gun (as designed into thermionic rf guns) and subsequent emittance growth. The LCLS gun will incorporate calibrated field probes in both cells to set and monitor the field ratio.

6.3.3 Symmetrization

The emittance growth due to multipole modes of E_z in a gun cavity with a conventional asymmetric rf coupler (as for the earlier BNL 1.5-cell gun) is estimated to contribute ~1 μm to the transverse emittance [22]. This growth is dominated by the dipole mode and the contribution from the higher order modes is less than 0.1 μm. Therefore the higher order modes can be neglected. Symmetrization in the prototype gun is achieved by including a second identical "coupling" hole (which is also used for vacuum pumping) directly across from the rf waveguide coupling hole. This reduces the field amplitude dipole term by an order of magnitude over the unsymmetrized case. Further symmetrization of the dipole field phase can be achieved by utilizing a symmetric power feed instead of a single-sided feed. This is done with a magic tee

along with two H bends that symmetrically feed rf power to the full cell of the LCLS 1.6-cell rf gun [23]. A diagnostics port in the magic tee will monitor rf power asymmetries. The coupling hole size will need to be reduced compared to the prototype gun to maintain the same rf coupling coefficient. Such a symmetric rf feed is planned for the LCLS gun.

6.3.4 120 Hz Operation

The prototype gun was originally designed for low repetition rates, but it is estimated that it could be operated up to 40 Hz. The stored energy in the cavity fields is 9.1 J for the LCLS design of 140 MV/m. The LCLS gun requires 14 MW of power from the klystron and has a filling time of approximately 670 ns assuming a Q_0 of 12000 and a critically coupled cavity resulting in an average heat load of 3.8 kW at 120 Hz. A slightly modified gun was designed and built by a BNL/KEK/SHI collaboration for operation up to 100 Hz [24]. Water cooling channels were added in the vicinity of the irises and satisfactory operation at 100 MV/m with a 4-μs wide rf pulse at 50 Hz has been demonstrated at the University of Tokyo at Tokai [25]. At these operating conditions the gun is dissipating roughly 1 kW of power.

At 120 Hz, the prototype gun with unmodified cooling channels would not operate at design specifications due to thermo-mechanical distortions. There are two possible solutions to this problem and some combination of the two will be adopted. The first solution, already utilized by the BNL/KEK/SHI collaboration, is to study the energy deposition in the rf gun and provide appropriate cooling at the optimal locations to minimize thermal gradients without compromising structural integrity [24]. One must also carefully consider the thermal distortions in the gun and not allow significant frequency shifts due to thermal expansion or introduction of higher order modes due to asymmetric cavity distortions.

Alternatively the thermal load can be reduced by a factor of three or more, i.e., to less than the 1-kW level already tested at Tokai, by properly shaping the rf pulse [26] and/or overcoupling the cavity to reduce the filling time. An overcoupled cavity with coupling coefficient of 1.5 instead of unity will dissipate 20% less power while only requiring 4% higher peak rf power to achieve an identical field in the gun. Using 30 MW of rf power instead of 14 MW to drive the gun, the rf field will build up to the desired value of 140 MV/m in only 750 ns instead of 2.8 μs. Once the desired accelerating voltage is reached, a fast (100 ns) rf attenuator on the klystron input could be used to stabilize the voltage at the desired value during beam extraction. The total rf pulse duration can thus be limited to about 1 μs with a corresponding reduction in the heat load of a more than a factor of three.

6.3.5 Photocathode

The choice of cathode material is a function of several restrictions including gun emittance, laser power at a given wavelength, longevity under rf processing or operation, and gun cavity construction. The use of a cathode plug or insert in an S-band gun has so far limited the cathode field to about 110 MV/m [27], whereas simulations indicate the transverse emittance drops with increasing field up to about 140 MV/m. However, a load-lock coupled gun, which utilizes a back

plane that is replaceable under vacuum, should eliminate this restriction. Such a system allows greater flexibility of cathode choice and easy upgrades as improved materials are realized.

A metal photocathode is chosen for the preliminary configuration for several reasons. Since the source is not required to produce a bunch train (multiple microbunches within each pulse), the lower QE of metal cathodes compared to alkali and semiconductor photocathodes is not a major concern. The QE for Cu illuminated with UV light at normal incidence depends on surface preparation, but a QE of 10^{-5} at 260 nm (4.77 eV) in a non-load-locked gun is achievable. See **Section 6.2.1**, *Quantum Efficiency*, and also references [28,29,30]. Much better QE is available from copper installed through a load-lock. This is illustrated by the data of **Figure 6.11** for which a carefully prepared polycrystallline Cu photocathode was inserted into an ultra-vacuum surface analysis chamber using a load-lock (no baking) and the QE spectrum measured at low voltage [31]. The figure shows a QE of 2.3×10^{-4} at 266 nm.

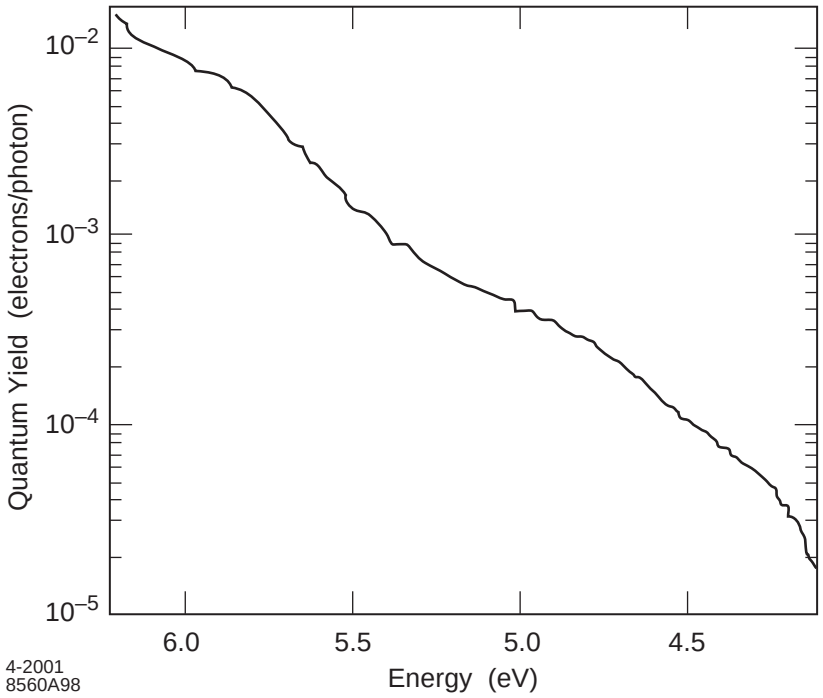

Figure 6.11 Copper QE as a function of quantum energy measured with low (22 V) dc bias with the surface untreated after installation in the analysis system using a load-lock. Photon wavelength in nm is equal to 1240 divided by the energy in eV; i.e., at 4.8 eV the wavelength is 260 nm.

A gain in QE by a factor of two to four can be achieved by illuminating the cathode at a grazing angle This gain is primarily due to the increased absorption of *p*- over *s*-polarized light [32], but its benefits are partially offset by the laser energy lost in shaping the pulse for grazing incidence.

At 260 nm, an optical pulse of 500 μJ on the cathode is required to produce 1 nC of charge when the QE is 10^{-5}. A laser system to meet this requirement is relatively straightforward to design. (See **Section 6.4**, *Laser System*.)

At extremely high photon intensities, the metal surface will begin to disintegrate. Even with such disintegration, the QE of the cathode tends to remain high, presumably due to the enhancement of field emission along the surface disruptions. However, a large and undesirable increase in dark current accompanies such a surface [33]. The photon intensities planned for the operation of the LCLS source are well below this regime.

The principal advantages of metal cathodes are that they are easy to fabricate and that the entire end plate of the half cell can be formed in the standard manner of Cu rf cavities, permitting operation at the highest field values. The photoelectric response time of metal cathodes is on the sub-picosecond level, thus imposing no limitation on the desired temporal pulse shaping.

The QE for a magnesium photocathode is about one order of magnitude higher than for Cu prepared in a similar manner [34,35]. The higher QE for Mg is attributed to its lower work function. For a given excitation energy, a lower work function implies a higher thermal emittance, which could be a limiting factor for a low emittance beam. However, if one considers threshold emission, i.e., emission in which the excitation energy is barely above the work function, the QE for Mg presumably would be roughly equal to that for Cu. However, since the laser wavelength for Mg would be much longer than for Cu, there would be a definite system advantage to Mg. For this reason, and since the QE of Mg cathodes for threshold emission is potentially higher than for Cu, the search for a way to use a Mg cathode with fields on the order of 120 MV/m—including how to fabricate a high rf-field removable plug—will continue. A load-lock system is particularly useful for Mg because of magnesium's extreme chemical reactivity to water vapor. A Mg plug can be embedded into a copper cathode plate, finish polished in a dry-nitrogen or argon glove box and transferred in-situ to the photocathode vacuum storage vessel for later transfer, under vacuum, into the gun.

6.3.6 Emittance Compensating Solenoid

For emittance compensation, a solenoid with precisely defined field symmetry and positioning will be used at the gun exit. The solenoid design for the prototype gun incorporates several pancake assemblies, each assembly including a pancake coil and steel flux straightener as well as alignment components. Conventional manufacturing techniques using molded coils do not accommodate the required flux straightener position accuracy, therefore the straighteners are positioned independently of the coil positioning. The physical length of the solenoid assembly is 22.5 cm including the flux return, while the pancakes themselves are 19.5 cm. A map of the measured axial magnetic field is shown in **Figure 6.12**. The solenoid incorporates steel flux returns to reduce the field at the cathode to approximately 5 Gauss, negating the need for an identical bucking coil behind the cathode to null the field at the cathode plane. This solenoid design allows for a much simpler design of the load-lock system.

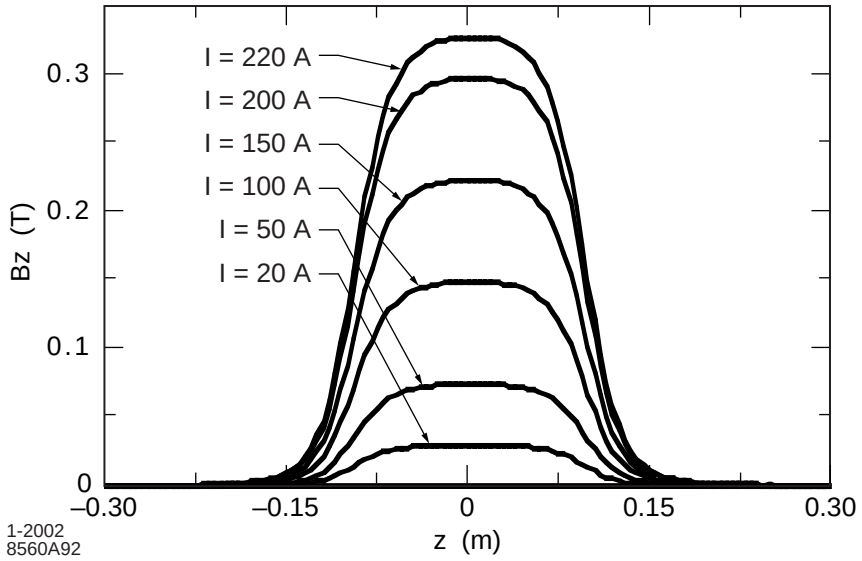

Figure 6.12 Measured axial magnetic field of the emittance compensation solenoid as a function of distance z along the axis. In this figure, z is referenced to the center of the solenoid. The peak value of B_z increases as the solenoid current, I, increases.

6.3.7 Vacuum System

After brazing and before final tuning, the rf gun will undergo a 450°C vacuum bakeout in the SLAC Klystron Department's vacuum bakeout facility. This procedure removes excess hydrogen absorbed by the vacuum surfaces of the rf gun during brazing. Ion-NEG pumps (separate or combined) will be located in the rf waveguide near each of the two rf input couplers at the gun (the gun vacuum is separated by the rest of the rf waveguide by rf windows) and also in the beamline just downstream of the emittance compensating solenoid. Small 20 l/s ion pumps will be used in the waveguide, while a large 220 l/s ion pump will be in the beamline. Together these pumps should provide a pressure of $\leq 5\times10^{-10}$ Torr at the gun with the field gradient at its normal operating strength and the rf at 120 Hz. The 220 l/s pump also maintains the vacuum in the diagnostic section following the gun.

A schematic of the proposed LCLS gun assembly is shown in **Figure 6.13**. A load-locked cathode storage and transport system is coupled to the rear of the gun. Through use of isolation gate valves, the load-lock has a number of advantages over a non-load-locked system:

1) Photocathodes are exchanged under vacuum without exposure to atmospheric (particularly the gun vault) environment. This eliminates the oxidation, dust accumulation, and carbon contamination onto the cathode surface that usually results from exchanging cathodes when opening the rear of the gun to ambient atmosphere.

2) The gun is not exposed to atmosphere in the cathode exchange procedure, therefore a bakeout of the gun itself is not required following the exchange.

3) Processing of the cathodes takes place ex-vault where the cathodes will be polished under inert atmosphere (in the case of Cu or Mg), deposited in vacuum (in the case of Cs_2Te),

or plasma-cleaned of carbon. In each instance, the processed cathode is subsequently moved in-situ to a cathode storage chamber, ready for attachment to the gun load-lock.

4) Through the use of multiple "transport/storage" vessels, any number of cathodes can be prepared and stored long-term, under vacuum, then installed rapidly as needed.

The load-lock/photocathode gun assembly is shown in **Figure 6.13** with three sequential positions of a cathode plate: (1) loaded into the gun, (2) transported from the storage chamber to the gun transport chamber, and (3) in storage and attached to the gun load-lock.. Experience with the load-lock system of the SLAC Polarized Electron Gun shows that the entire process takes less than one shift (excluding any in-vacuo high-field processing of the new cathode, if needed).

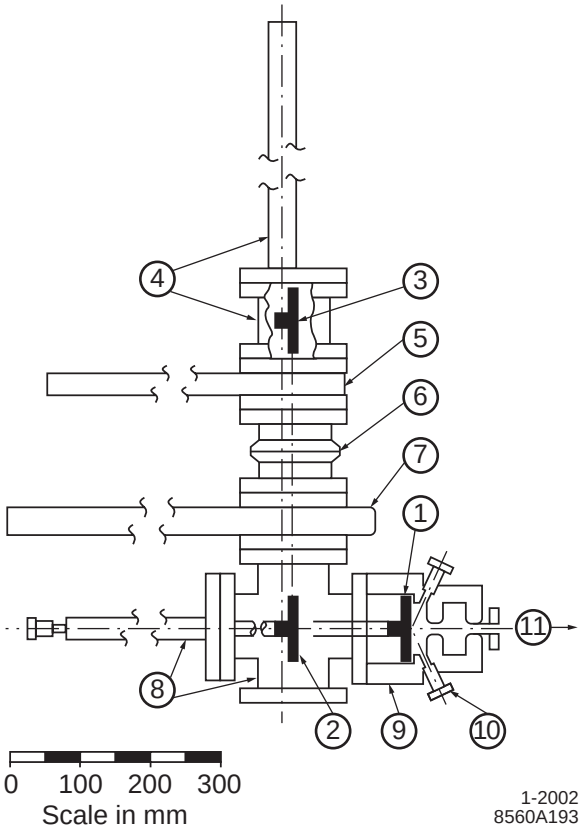

Figure 6.13 Schematic of photoinjector gun assembly showing vacuum transfer apparatus (load-lock) for cathode exchange. A photocathode (PC) plate is shown in it's three locations of the exchange process. The numbered components are: (1) PC plate in gun, (2) PC plate in transfer chamber, (3) PC plate in storage chamber, (4) storage chamber with transfer motion, (5) storage chamber gate valve, (6) quick-connect flange, (7) gate valve, (8) PC-exchange chamber with transfer motion, (9) rf photocathode gun, (10) laser light ports, (11) LCLS beamline.

6.4 Laser System

The laser system for the electron source is required to deliver a 500 μJ pulse of UV photons to the photocathode at a repetition rate of 120 Hz. To meet the emittance requirements of the

source, the laser pulse must have an adjustable pulse length and temporal shape, nominally a flat pulse 10-ps long, and a uniform transverse profile with an adjustable radius, nominally a hard edge at 1.0 mm. Finally, stability is an important operational requirement, and, as discussed in **Chapter 7**, the timing stability in particular is crucial to meeting the energy stability requirements in the undulator. **Table 6.3** summarizes the laser's design requirements.

6.4.1 System Description

The titanium-sapphire laser system of **Figure 6.14** provides the ultraviolet light pulses for the rf gun. This system is first described briefly; subsequent sections then elaborate on various aspects of the design.

A CW, frequency-doubled, diode-pumped Nd:$YV0_4$ laser provides highly stable energy in the green (532 nm) to pump the CW mode-locked Ti:sapphire oscillator, which then delivers a stable, continuous train of 12-nJ, 100-fs FWHM pulses that repeat at 79.33 MHz. This frequency, the 36^{th} subharmonic of the linac's 2856-MHz rf, locks the timing of the laser pulses to the phase of the rf in the linac and rf gun. The wavelength is tuned to 780 nm, near the peak for Ti:sapphire output. This frequency is tripled to 260 nm after amplification to provide a suitable wavelength for the photocathode of the gun. With some reservations about timing stability (see **Section 6.4.7**, *Stability of Laser Pulse*), oscillators of this type are commercially available (e.g., the Spectra-Physics π-mode ®*Tsunami*).

Table 6.3 Laser System Requirements.

Parameter	Requirement
Operating wavelength	260-270 nm (for Cu cathodes)
Pulse repetition rate	120 Hz
Number of micropulses per pulse	1
Pulse energy on cathode[a]	>500 μJ
Laser spot radius on cathode[b]	0.71 mm rms
Pulse rise time (10-90%)	0.5 ps
Pulse length	2.9 ps rms
Longitudinal pulse shape	Various, but nominally uniform
Transverse pulse shape	Various, but nominally uniform
Homogeneity on cathode	10% ptp
Optical energy jitter (in UV)	≤2% rms
Laser-to-rf phase jitter	≤0.5 ps rms
Laser spot diameter jitter at cathode	1% peak-to-peak
Pointing jitter	<1% of radius rms

a The design will be for 18 mJ of IR energy just after the amplifiers, resulting in at least 500 μJ available at the cathode. For a QE of 10^{-5}, 500 μJ of excitation light at 260 nm at the cathode will produce 1 nC of charge.

b For a uniform, round, transverse cross section, the hard-edge radius, r_c, is related to the rms radius, σ_r, by $r_c = \sqrt{2}\sigma_r$. In this case, if σ_r is 0.71 mm, r_c would be 1 mm.

c For a uniform temporal cross section, the edge-to-edge pluse length, l_c, is related to the rms length, σ_t, by $l_c = \sqrt{12}\sigma_t$. In this case, if σ_t is 2.9 ps, then l_c would be 10 ps..

A Pockels cell and polarizer are used to gate single pulses at 120 Hz from the 79.33-MHz pulse train. The selected pulses are then amplified by two Ti:sapphire crystals, both configured as 4-pass "bow-tie" amplifiers [36]. Both are pumped by a pair of Q-switched, doubled Nd:YAG lasers that fire in alternation, each producing a 60-Hz train of 3 to 10-ns pulses. Again, commercial lasers (such as Coherent's ®*Infinity* or Spectra-Physics' ®*Quanta-Ray PRO*) with an additional feedforward loop to decrease amplitude jitter will be used as discussed later in the

section on stability. Fourier-relay optics (described below), beginning with a primary aperture between the two amplifiers and continuing to the final optics platform next to the gun, are used to maintain a good transverse mode while efficiently filling the pumped volume of the Ti:sapphire crystals.

In amplifiers for picosecond and especially sub-picosecond pulses, the peak power must be limited to avoid damage to optical components and nonlinearities. Chirped pulse amplification [37] is used to reduce the peak power in the amplifier. The large bandwidth of the Ti:sapphire oscillator, which enables it to produce the 0.5-ps rise time required for the shaped pulse, also permits the pulse to be stretched to hundreds of picoseconds. In the dispersive region between a pair of gratings, different wavelengths take different optical paths. The resulting space, time, and wavelength correlations are then used to stretch the pulse. After amplification, the process can be reversed to compress the pulse to the original or any greater width. In addition, the oscillator's large bandwidth allows the pulse to be shaped in time by manipulating its Fourier transform under computer control (see below). **Figure 6.14** includes the pulse shaper and stretcher after the oscillator and a compressor after the amplifier. An additional low-power compressor after the oscillator is used as a diagnostic for the pulse shaper. It compresses the pulses from the 89-MHz train that are not selected by the Pockels-cell gate. A cross-correlator using a portion of the oscillator light can then probe the resulting pulse shape.

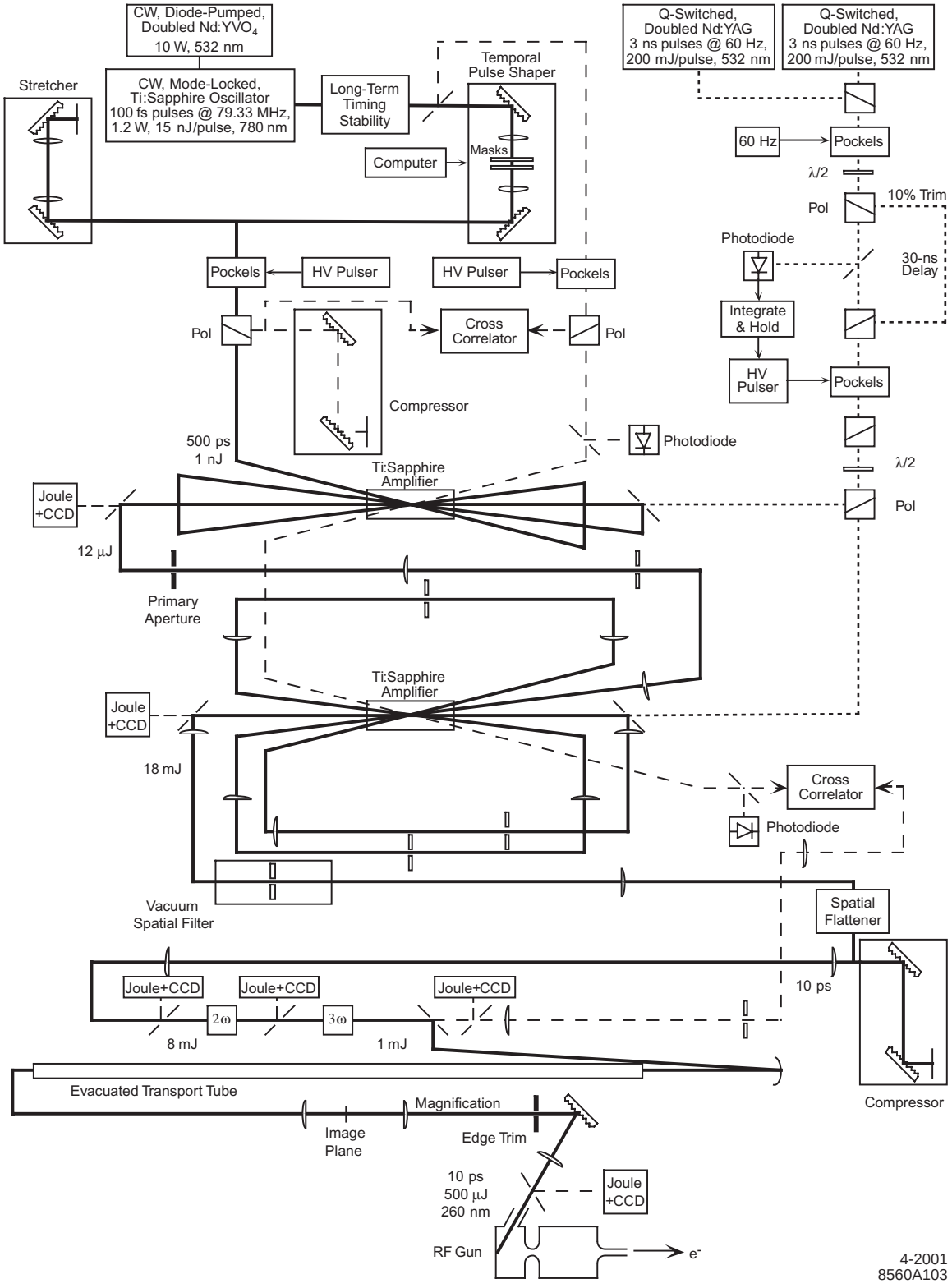

Figure 6.14 The drive laser for the rf photocathode electron gun for the LCLS. The thick lines show the main beam path, the widely spaced, dashed lines indicate diagnostic beams, and the closely spaced, dashed lines are pump beams.

After the second amplifier, the transverse shape of the pulse is modified from Gaussian to uniform to better match the requirements for obtaining a low emittance from the gun. Next, two crystals triple the frequency of the light to a wavelength of 260 nm. The flattened pulse also improves efficiency and uniformity in this harmonic-generation process.

Finally, the beam is transported through an evacuated tube to an optics platform next to the gun. Since the Fourier-relay image plane that follows the long transport tube has a spot size that is too small for the photocathode, the spot is magnified by imaging it onto a circular aperture that slightly trims the edge of the beam. This aperture is in turn imaged onto the photocathode, so that the illuminated region of the photocathode is precisely defined without jitter. The imaging includes compensation (discussed below) for the temporal and spatial distortion caused by grazing incidence on the photocathode.

The energy management of the laser system, also indicated in **Figure 6.14**, is as follows: transmission through the spatial flattener is 50-75% (with ~100% a real possibility using the aspheric optics mentioned in **Section 6.4.4**, *Spatial Pulse Shaping*), through the compressor 50-65%, through the frequency tripling stage 10-15%%, and through the optical transport to the gun 50% for an average overall IR to UV efficiency of 2.7%. Consequently, starting with 18 mJ after the second amplifier, the required 500 μJ is delivered to the cathode.

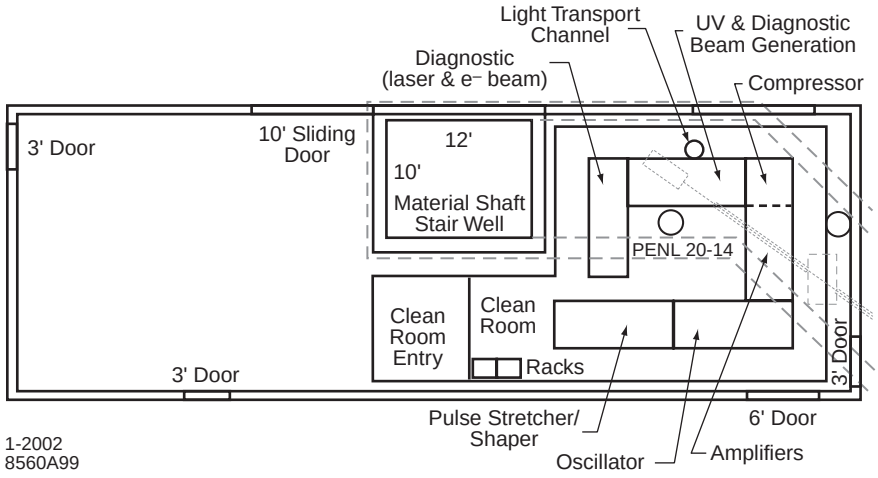

Figure 6.15 The surface building alongside the Klystron Gallery at Sector 20 showing the layout of the laser clean room. The injector vault below is dashed in.

The design actually calls for two complete laser systems. The second system will be a ready spare and also allow implementation of upgrades and conduction of short performance tests while the LCLS is operating with the first system. Many of the advanced features of the laser will need commissioning and no doubt will undergo improvements as time goes on. Meanwhile, light to the photocathode must be delivered to begin commissioning the rest of LCLS. The clean room for the

laser, shown in **Figure 6.15**, will have optical tables for the two systems, so that one laser can deliver beam while the other is on standby, being repaired, or being used for further development. To provide for enhanced system reliability, the two lasers will be set up so that either will be able to send light to the photocathode in the vault below. An additional table provides space for shared diagnostics, like a streak camera.

6.4.2 Temporal Pulse Shaping

The spatial and temporal shape of the optical (and thus also the electron) pulse is nominally Gaussian. However simulations indicate that an emittance-compensated beam at the exit of the injector will have a lower transverse emittance if uniform temporal and spatial distributions of charge are extracted at the photocathode. As the beam makes its way through the linacs and compressors, simulations indicate that the bunch length at the entrance to the undulator is more sensitive to timing jitter when the beam starts with a uniform rather than a Gaussian temporal shape. To permit the injector pulse shape to be optimized for the lowest possible emittance, a short X-band accelerating section is introduced just before BC1 to linearize the compression independently of the L0 pulse shape. (See **Section 7.2.3**, *X-band RF Compensation*.) However, since an experimental variation of the pulse shape will be needed to establish the final optimized configuration, the capability to shape (including a uniform shape) the temporal profile of the laser pulse is built into the system.

Temporal shaping of the optical pulse will be accomplished through the well-established technique of frequency-domain pulse shaping [38], which takes advantage of the large bandwidth of ultrafast laser pulses. The electric field of an ultra-short laser pulse with a Gaussian temporal envelope can be written as

$$E(t) = E_0 e^{j\omega_0 t} e^{-\left(t/\sqrt{2}\tau\right)^2} . \qquad \textbf{(6.7)}$$

The pulse bandwidth is determined by the Fourier transform of this field, where the Fourier transform is

$$E(\omega) = \frac{1}{\sqrt{2\pi}} \int_{-\infty}^{+\infty} E(t) e^{-j\omega t} dt . \qquad \textbf{(6.8)}$$

The power spectrum is then

$$E^2(\omega) = E_0^2 \tau^2 e^{-(\omega_0 - \omega)^2 \tau^2} , \qquad \textbf{(6.9)}$$

where τ is the *1/e* half width of the laser pulse intensity. For a Gaussian distribution of locked oscillator modes, the spectral full width at half maximum, $\Delta\omega$, is related to τ as $\Delta\omega \approx 1.67/\tau$. Thus the shorter the pulse the larger is the spectral bandwidth.

The frequency spectrum is dispersed in space between a pair of diffraction gratings separated by a pair of lenses. Relay imaging between the gratings avoids introducing time dispersion in this section. Spatially resolved amplitude and phase masks at the dispersion plane modify the Fourier

transform of the laser pulse and permit any pulse shape allowed by the bandwidth to be produced. In principle, one can make a square pulse with a rise time equal to the pulse duration of the original pulse. In **Figure 6.14**, the gratings and masks for pulse shaping are located between the oscillator and the first amplifier stage. This arrangement reduces the possibility of damage to the pulse shaping optics. The pulse shape will subsequently be modified by the gain properties of the amplifiers and the frequency conversion process. Thus, the Fourier transform produced by the masks and gratings must take these changes into account. To accomplish this, the amplitude and/or phase masks will be made with computer-addressable liquid-crystal optics [39]. Linear liquid-crystal arrays designed for this purpose have become commercially available [40]. Pulse-shape measurements then allow feedback on the mask configuration, modifying it to produce the desired shape. Thus, the effects of frequency conversion and gain shaping will be readily taken into account, and it will be relatively simple to change the pulse shape if another is found to be advantageous.

6.4.3 Fourier Relay Optics

A technique known as Fourier relay imaging combines relay imaging, in which lenses form an image of an initial aperture at each pass through a subsequent amplifier or harmonic-generation crystal, with the filtering of the beam's spatial Fourier transform. This approach can maintain a clean transverse mode and improve pointing stability, while also achieving better utilization of the pump energy. Initially, the oscillator beam is trimmed in an aperture. At each step a lens of focal length f_1 is placed a distance f_1 after one of the image planes. The Fourier transform is formed at the focus f_1 beyond the lens, where a pinhole removes higher spatial harmonics. A second lens with focal length f_2 then recollimates the beam (with magnification f_2/f_1) and forms the relay image at a distance $2(f_1 + f_2)$ from the previous image plane. Similar imaging takes place at the harmonic-generation crystals, and finally an image of the aperture is relayed to the photocathode to define the area of photoemission. The relay lenses and pinholes are indicated in **Figure 6.14**.

6.4.4 Spatial Pulse Shaping

To shape the pulse in space, a position-dependent attenuation will be applied to the beam [41]. The demonstrated use of low loss aspheric refractive optics to *flatten* Gaussian profiles with ~100% efficiency also shows promise [42]. Relay imaging must be used *after* the flattening, to limit diffraction. Since repeated filtering of the spatial Fourier transform would limit the steepness of a flat-top output pulse, Fourier filtering is not incorporated in the imaging after the spatial shaper. Also, flattening is generally lossy, and so the system must have sufficient gain. On the other hand, harmonic generation can be more efficient with a uniform intensity across the beam.

6.4.5 Frequency Conversion

The 780-nm pulses will be frequency tripled to 260 nm in a pair of frequency conversion crystals using Type-II–Type-II tripling [43]. In this polarization-mismatch scheme, the beam is

detuned from optimal conversion in the first crystal in order to allow efficient conversion to the third harmonic in the second. In Type II doubling, the beam is typically incident with a polarization angle of 45° with respect to the e- and o-axes. For polarization mismatch, the beam is polarized at 35° with respect to the o-axis, allowing approximately 50% conversion to the second harmonic. The unconverted fundamental beam is mixed with the converted beam in the second crystal. Frequency conversion efficiencies in excess of 50% to the third harmonic have been measured with picosecond 1-μm laser pulses. A pair of BBO (beta-BaB_2O_4) crystals with phase matching angles of 42° and 54° respectively is proposed. The conservative energy estimates of **Figure 6.14** assume a day-to-day tripling efficiency of 25%, although twice this efficiency should be achievable.

In general, the intensity and wavelength dependence of frequency conversion can give rise to pulse distortion. However, frequency conversion will maintain the shape of our temporally and spatially uniform pulse (a cylindrical slug), and will allow the conversion efficiency to be optimized. The nonlinearity of the process can also sharpen the edges. On the other hand, an initial non-uniform shape will be distorted during conversion, and this must be accounted for in generating the input pulse shape. In addition, any structure on the pulse—ripples in time or space—can grow during the conversion process, again due to the nonlinearity [44]. This means that the constraints on the spatial and temporal uniformity before conversion will be more severe than those required at the photocathode.

6.4.6 Grazing Incidence

In the rf photocathode guns developed by the Brookhaven-SLAC-UCLA collaboration, the laser can be incident on the photocathode at either normal or near-grazing incidence (72° from the normal). Measurements at SLAC [45] using grazing incidence, in which the UV light was changed from *p*-polarized (electric field nearly normal to the surface) to *s*-polarized (*E* parallel to the surface), have shown 5 to 6 times more photoemission for *p*. Part of this improvement, a factor of 2.5, is due to the lower reflectivity for *p*; the balance is attributed to the Schottky effect. Since the reflectivity is enhanced for normal incidence, the emission should be about half when compared to grazing incidence with *p* polarization. Similar work at UCLA [46] showed the same effect, but with somewhat lower enhancement due perhaps to a lower rf field in the gun. An additional advantage of grazing incidence is that there is no need to insert a laser mirror directly downstream from the gun, right next to the electron-beam path, where it is a potential obstacle and a source of wakefields. The LCLS gun design allows either method.

However, grazing incidence introduces two geometric difficulties: a circular laser beam incident at a grazing angle illuminates an elliptical spot on the cathode. Also, if the spot is millimeters across, the side closer to the laser entry will emit picoseconds earlier than the other side. Corrections for both of these effects are needed to minimize emittance. The elliptical spot is made circular in the last relay of the beam in **Figure 6.14**, from the final image plane to the cathode. Here, the light reflects from a diffraction grating with a groove spacing and angle of

incidence chosen to apply a compensating anamorphic magnification (different horizontally and vertically) and so illuminate a circular area.

A second constraint on the groove spacing and incidence angle provides a simultaneous correction of the time slew by adding a delay that varies across the beam (that is, by tilting the wavefront). By placing the grating in the beam near the final image plane, the time delay is correlated with the position across the cathode. Since gratings are lossy in the ultraviolet, care must be taken to make the beam size on the grating large enough to avoid damage.

6.4.7 Stability of Laser Pulse

6.4.7.1 Pulse-to-Pulse Timing

If the rms timing jitter of the electron bunch with respect to the rf driving the gun and linac is 1.4 ps measured over a few seconds at 120 Hz, then the energy of the beam in the undulator will vary by 0.1% rms. See **Table 7.4**. However, when all sources of energy jitter are taken into account, the rms timing jitter at L0 must be reduced to about 0.9 ps. See **Table 7.5**. A criterion of ≤0.5 ps rms has been adopted for the LCLS photoinjector laser system as indicated in **Table 6.3**.

Almost all of the laser system's jitter originates in the oscillator. An rms jitter of ≤0.5 ps has been measured on advanced commercial oscillators, such as the Spectra-Physics ®*Tsunami* described earlier, or the Time-Bandwidth Products Nd:glass laser used at SLAC's Gun Test Facility. However, while 0.5-ps performance has been measured, the manufacturers have not made this their standard specification; considerable care is necessary to maintain such performance. These lasers use sealed housings, mechanical stabilization of the optical platform inside, and precise electronics to lock the cavity length to an external rf reference. Careful attention must also be paid to isolating the housing thermally, mechanically, and acoustically on the optical table.

In order to assure both short- and long-term stability, the laser system presented here has its timing stabilized twice. The arrangement is illustrated in **Figure 6.16**. The first technique is incorporated in the commercial oscillators that are being considered. A measurement is made of the laser oscillator's output phase with respect to rf from the accelerator's main rf drive line. The phase-error signal, which is first low-pass filtered and then amplified, drives a piezoelectric translation stage holding the end mirror of the laser oscillator. The oscillator incorporates a passive mode-locker (using a Kerr lens or Fabry-Perot saturable absorber), while the length of the oscillator cavity, initially set up to match a subharmonic of the accelerating frequency, is continuously adjusted to lock the phase of subsequent laser pulses to the rf. The bandwidth of the method is estimated to be in the kilohertz range.

Outside the oscillator cavity, the timing is then corrected for long-term drift. A prism is mounted on a piezo stage with a fast motor to provide an optical-trombone delay for the laser pulses. As shown in the figure, this delay is controlled by a similar phase-error to that used for the stage inside the oscillator, but using 2856 MHz for greater sensitivity. It could additionally use

the measured phase error of the pulses of electrons or ultraviolet light with respect to the rf, as shown in the figure. Both the piezo and motor are computer controlled.

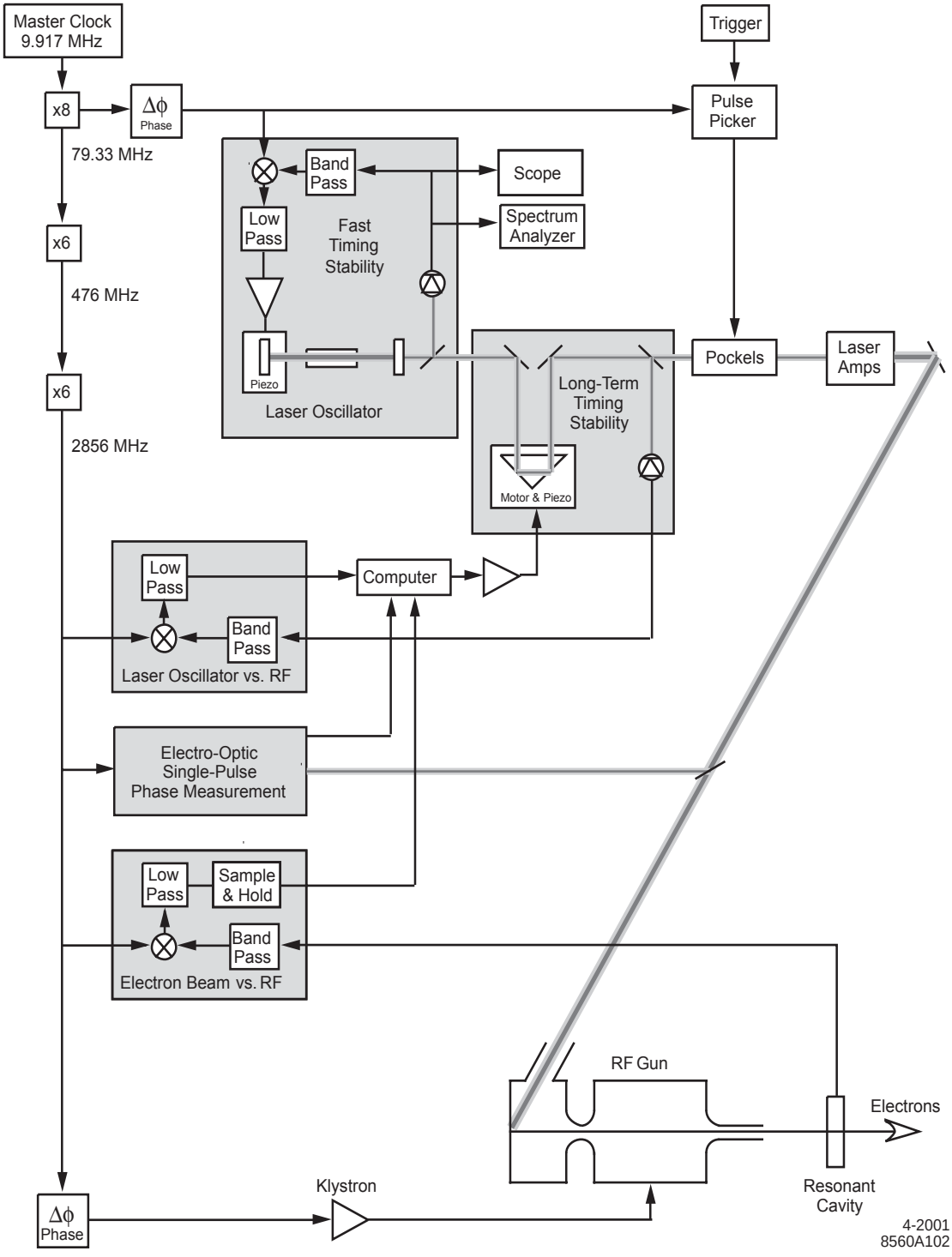

Figure 6.16 Timing stabilization schematic.

6.4.7.2 Pulse Duration

Like timing jitter, the stability of the pulse duration is important for LCLS performance. The pulse duration should fluctuate by no more than the allowable timing jitter. A stable oscillator is again essential. If the bandwidth of the oscillator pulse is wider than that transmitted by the phase and amplitude masks used to shape the pulse in time, so that the masks are illuminated almost uniformly, then fluctuations in the oscillator width have little effect on the final pulse length or shape. The latter are determined only by the masks and the pulse compressor following the amplifiers.

6.4.7.3 Optical Energy

If the optical energy and thus the charge at the photocathode varies with an rms value of 6% over a period of a few seconds at 120 Hz, the contribution to the peak charge jitter in the undulator will be at the LCLS limit of 12%. See **Table 7.4**. However, when all sources of charge jitter are taken into account, the rms optical energy at the cathode is required to be ≤2% (see **Table 7.5)**. Thus a criterion of ≤2% rms (in the UV) has been adopted as indicated in **Table 6.3**. Harmonic generation compounds the difficulty of this criterion, since 2% jitter in the third harmonic requires 0.7% stability in the fundamental. It is difficult for a Pockels cell to trim the amplitude of a broadband pulse without affecting its temporal shape. Thus the UV energy at the gun is stabilized by using laser-diode pumping in the oscillator, by carefully controlling the beam mode and its pointing through the amplifiers through Fourier relay imaging, and by stabilizing the amplifier pumping with feedback.

The older generation of Ti:sapphire oscillators, both CW and mode locked, were pumped by green light from argon-ion lasers. In the newer generation, these have been replaced by diode-pumped, frequency-doubled Nd:YVO_4 lasers, which have far lower noise. With 10 W of green, the pumps from both Spectra-Physics (®*Millennia Xs*) and Coherent (®*Verdi-V10*) have a rated noise (above 10 Hz) below 0.04% rms. Most of this performance carries forward to the Ti:sapphire output, although there are some differences in how the manufacturers have tightened their specifications since moving to the new pumps. At the LCLS wavelength, an output power of at least 1.2 W with rms noise of 0.1% or less is expected.

To control the amplifier's pumping, the relatively long upper-state lifetime of Ti:sapphire (3.2 μs, long compared to the few-nanosecond duration of the pump pulse) will be used to hold the total pump energy constant on every pulse. The pump beam has an rms jitter of about 2.2% (for the ®*Infinity* delivering 200 mJ of green at 60 Hz) to 3% (for the ®*Quanta-Ray*, which can deliver more than 300 mJ and so provides some "headroom"). These pump lasers have maximum repetition rates of 100 Hz. To obtain 120-Hz pumping for LCLS, we use a polarizer to merge the beams from two frequency-doubled Nd:YAG lasers operating in alternation at 60 Hz (Figure 6.4-1). One beam enters with vertical polarization, the other horizontal. After the polarizer, a Pockels cell pulsed at 60 Hz rotates the vertically polarized beam to create a 120-Hz train with horizontal polarization. (This scheme has the additional feature that a failure of one pump cuts the repetition rate in half, rather than stopping LCLS completely.) The jitter will be corrected by picking off 10-

15% of the beam, enough to correct the jitter, which is then delayed by a 30 ns optical path. This delay gives time to adjust the high voltage on the Pockels-cell of **Figure 6.14**. Based on a measurement of the energy in the pump pulse, a portion (nominally half) of the delayed light is added back into the pump path, so that the pumping of the Ti:sapphire is trimmed for each pulse by up to ±5%. The pump has a narrow bandwidth, unlike the temporally shaped Ti:sapphire beam, and so it is easily trimmed by the Pockels cell. The full pump beam is not trimmed, because at 50% transmission a Pockels cell with a polarizer is in the linear part of the control range, while at 95% the curve is flat and nonlinear; a much larger voltage swing would be needed to effect the same change.

To correct for long-term drift in the UV pulse energy as monitored at the gun, a slower software feedback loop will adjust the set point in the faster feedback loop that stabilizes the amplifier pump energy.

6.4.7.4 Spot Size and Position

To carefully and reproducibly control the distribution of space charge in the gun for optimal emittance, the laser must maintain a 1% variation in the diameter of the laser spot on the photocathode with a centroid location that varies by no more than 1% of the diameter. Position stability will be achieved by trimming the edge of the beam with a circular aperture placed on the final relay-image plane before the gun; this aperture is then imaged onto the photocathode. A Gaussian beam could still have fluctuations in the position of its centroid within the aperture, but with the uniform pulse shape preferred for LCLS, pointing jitter does not cause any change in cathode illumination (as long as the full beam-trimming aperture is illuminated, despite the jitter).

6.4.8 Laser System Diagnostics

The laser system is designed with an integral diagnostic beam. (See **Figure 6.14**.) This beam is used to monitor the shot-to-shot amplifier gain and also is used for diagnosing the temporal shape of the UV pulse heading toward the photocathode. To obtain the diagnostic beam (narrowly spaced dashed line in the figure), a Pockels cell and polarizer gate a second oscillator pulse that follows the primary pulse by tens of nanoseconds. The diagnostic pulse makes only one pass through each of the amplifiers. A photodiode measures its energy at each stage to check the gain. The unstretched (100 fs) diagnostic pulse is then cross-correlated with the UV output pulse (3 10 ps) to measure the pulse shape.

6.4.8.1 Cross-correlation Pulse Shape

The advantage of using a diagnostic beam for a cross-correlation measurement of the UV pulse is that the diagnostic beam retains the original 100-fs duration of the seed beam and so provides a comparable temporal resolution. Cross-correlation provides more information than an auto-correlation because the latter cannot distinguish temporal asymmetries. The diagnostic pulse will be chosen to arrive at a cross-correlator at the same time as a fraction of the primary pulse picked off by a beam splitter. There are a number of techniques for measuring the cross-correlation of an infrared and UV pulse. It is anticipated that a single-shot polarization-gating

cross-correlator [47] will be used. This will generate a third-order intensity cross-correlation of the 100-fs, 780-nm IR pulse and the 10-ps UV pulse. If the IR pulse is used as the gating pulse, the measured pulse shape is that of the UV pulse with a temporal resolution of approximately 100 fs. The two pulses are incident nearly collinearly on a nonlinear optic. The UV pulse to be detected is incident on a spatially resolving detector through crossed polarizers. In the absence of a gating pulse, no UV light is detected. Between the polarizers there is a Kerr medium, such as a thin piece of fused silica. When the gate pulse is incident on the Kerr medium, it acts as in instantaneous waveplate, which allows the portion of the UV pulse passing through the same space-time location to pass through the crossed polarizers and be detected. By choosing the crossing angle, detector and crystal size, and appropriate probe-beam energy, the pulse duration can be measured with a resolution approaching the 100-fs duration of the gate pulse. In addition, by following the cross-correlator with a spectrometer, the frequency resolution is improved. This FROG (frequency-resolved optical gating) technique [48] allows both the temporal and phase profiles of the beam to be determined.

The effect of the pulse shaping on the low-energy IR pulse will also be measured using cross-correlation. In this case, all of the pulses (other than the pulse selected for amplification) from the 79.33-MHz train leaving the shaper and stretcher are selected. After recompression, their shape is measured in the cross-correlator shown in the low-energy area of **Figure 6.14**. The gating pulse comes from the diagnostic beam picked off before the shaper and stretcher. Again, all of the 79.33-MHz train is used except for the diagnostic pulse. Because both beams entering this cross-correlator are trains (except for the 120 pulses per second selected by the Pockels cells), it can use a simpler swept time delay to scan the overlap of the pulse trains, rather than the single-shot approach of the output cross-correlator, where different time delays occur at different spatial locations.

6.4.8.2 Energy

The energy will be monitored using joulemeter probes in combination with calibrated pick-offs at several points in the system: after each amplifier stage, after each harmonic conversion, and just before the beam enters the rf gun's vacuum to strike the photocathode. These checks allow simple monitoring of amplifier and harmonic-generation efficiency. Photodiodes will be used at other points where the pulse energy will be low.

6.4.8.3 Spatial Shape

The spatial shape of the beam on the photocathode will be monitored by picking off a fraction of the beam near the window leading into the gun. A CCD (without the usual protective glass cover, since it would block the UV laser light), placed at the pick-off image plane and at the same angle to the beam as the cathode surface, would then image the beam spot. (The pick-off image plane is optically the same distance away as the cathode but physically located outside the high-radiation area using an imaging fiber optic relay.) Typical CCDs are 4 to 9 mm wide, a good match for the spot needed on the cathode. For a grazing angle on the cathode, it is preferable to get a CCD on a printed circuit board rather than in a camera body since the body blocks the

correct angle. Alternatively, the UV could be incident on a fluorescing surface at the correct angle, and a CCD camera could record the visible glow; however, the response may be somewhat less uniform than that of a direct hit on the CCD. Other CCDs check the beam's transverse mode after each amplifier and at each harmonic-generation step.

6.4.8.4 Stability of Spot Centroid

The same CCD at the gun will measure the stability of the spot centroid on the photocathode. A computer with a digital frame grabber will record the video image, calculate the centroid location, and keep statistics on its stability. For each laser pulse, the centroid will be calculated to better than one pixel, which is typically 8 to 13 μm, about 1% of the typical 1.0-mm beam radius (hard edge). The mean and standard deviation can be calculated with even higher accuracy.

6.4.8.5 Timing Jitter

Most of the timing jitter is introduced in the laser oscillator. To measure it, some light is picked off with a fast photodiode just after the oscillator, as shown in **Figure 6.16**. Such diodes are available with rise times down to 7 ps. Time-domain measurements, using an equivalent-time sampling oscilloscope triggered by the rf of the gun, are limited to 2–3 ps resolution. In the frequency domain, the same photodiode pulse can be the input to a spectrum analyzer. The timing jitter can be determined from the differences of this spectrum at high and low harmonics using well known techniques [49]. Finally one can mix this diode signal with rf (as already done for the piezo controlling the oscillator's end mirror). The phase error (DC) can then be measured with an ordinary oscilloscope, studied in a spectrum analyzer to identify possible noise sources with narrow frequencies, and ultimately recorded by the accelerator control system.

A measurement of the laser pulse jitter with respect to the arrival of the electron beam itself is also possible at a BPM or resonant cavity in the beam-line near the gun exit. In a similar fashion the timing jitter of the electron beam itself with the rf can be also estimated as shown in **Figure 6.16.**

6.5 Electron Beamline

6.5.1 System Description

The overall layout of the photoinjector system in the context of the injector vault and accelerator housing is shown in **Figure 6.17**. The electron beamline consists of the rf gun (see **Section 6.3**), Linac 0 (L0, also referred to as the *booster* accelerator), and the Matching Section. The gun is followed by an emittance compensating solenoid. Linac 0 consists of two SLAC-type 3-m S-band accelerator sections separated by a drift space. A solenoid is wrapped around the first section, L0-1. (See **Section 6.1.3**, *Design Principles*.) Linac 0 is followed by a Matching Section (MS) that brings the beam from the injector vault to Linac 1 (L1) in the accelerator housing. The optical design of the MS, also referred to as "dog-leg" 1 (DL1), is described in **Section 7.5.1**, *Low-Energy Dog-Leg*. The design accommodates various diagnostics that are discussed in the following subsections.

Figure 6.17 also shows the new radiation shielding separating the injector vault from the linac housing. The injector personnel protection system is designed to allow access to the injector when the linac is operating (including 50-GeV beams), but electron beams in the injector cannot be run when the main linac is in permitted access. (See **Section 6.7,** *Radiation Protection Issues*.) Turning off the first MS bend magnet allows independent operation of the injector and main linac. In this situation, a spectrometer dipole in the aisle just beyond the main linac bends the injector beam into a beam dump, while the main linac supplies beam to the Research Yard (End Station A, etc.).

A schematic layout (not to scale) showing only the principal beamline elements is shown in **Figure 6.18**. The diagnostics are discussed in **Section 6.5.2**, *Standard Beamline Diagnostics*. Because of the unique nature of the LCLS photoinjector, there is also the need for several state-of-the art diagnostics. These are described in **Secs. 6.5.3**, *Slice Emittance*, and **6.5.4***, Temporal Pulse Shape*.

The rf distribution system is also shown in **Figure 6.18**. UnSLEDed klystrons will be used to improve the phase and amplitude stability. The accelerating sections will operate at about 25 MeV/m (see **Section 6.6**, *PARMELA Simulations*). The electron beam energy increment, E in units of MeV, in a standard SLAC 3-m section installed in the 3-km linac, is

$$E[MeV] = 10\sqrt{P[MW]}\,, \qquad \textbf{(6.10)}$$

where P is the klystron rf power at the klystron in units of MW. Thus the gun and each of the two 3-m sections require their own 5045 klystron. The rf deflector will also require a separate klystron. This arrangement will allow the rf phase and amplitude for the rf gun, the two sections, and the rf deflector to be controlled independently using low-power controls.

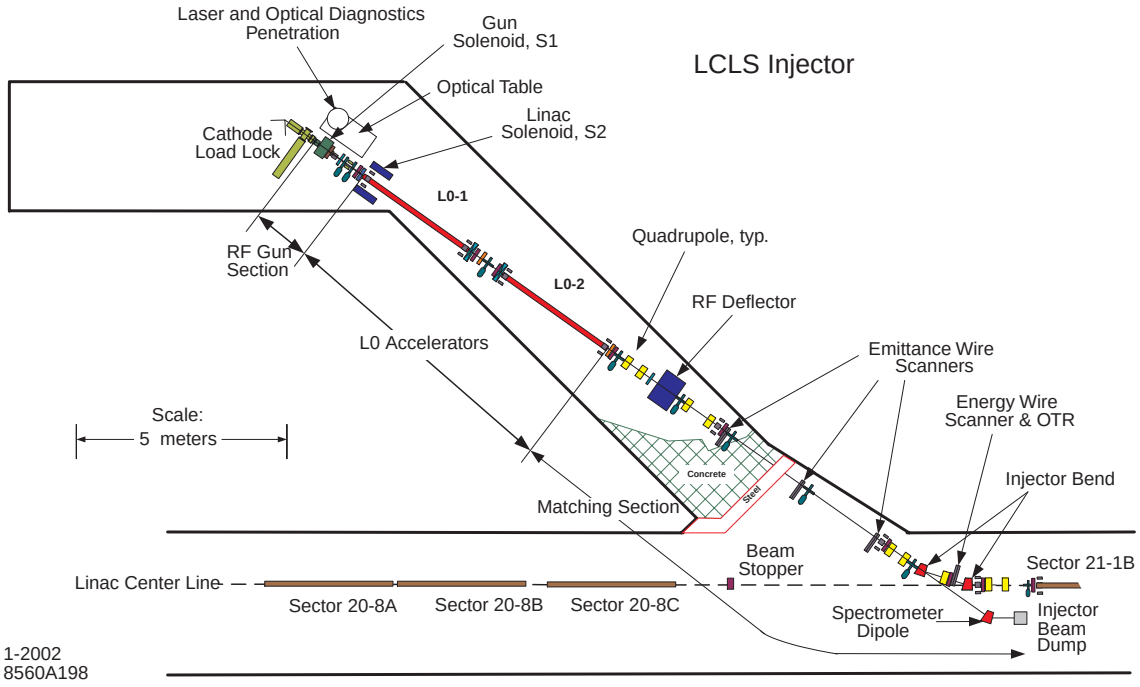

Figure 6.17 Scaled layout of the LCLS photoinjector in the Sector 20 off-axis injector vault of the SLAC 3-km linac. The rf gun and booster accelerator are at 35° to the main linac axis. This angle maximizes the injector length and gives access around the cathode load-lock.

Klystron 21-1 will not be needed for L1 since the corresponding accelerator sections will be permanently removed for Bunch Compressor 1 (BC1). The rf from this klystron will be rerouted to the rf gun. Klystrons 20-6, 20-7 and 20-8 are downstream of the positron source and thus are not used by PEP-II. During LCLS operation their rf will be rerouted to the rf deflector and to sections L0-1 and -2 respectively. Thus no new klystrons are needed for the injector.

The voltage for the modulators in Sectors 19 and 20 are presently controlled through the same variable voltage substation (VVS). The existing Personnel Protection System (PPS) works through this VVS. For the LCLS injector, a contactor could be added to each of the 3 modulators. These contactors could be used satisfy the PPS requirements for the LCLS injector vault in a manner similar to the linac injector vault at Sector 0 and the compressor klystrons for the Damping Rings. However, if part of Sector 20 is run on a time slot for PEP and the other part on a time slot for LCLS, there may be some jitter on LCLS modulators based on where PEP fires. An independent VVS for L0 will greatly reduce this jitter. An independent VVS negates the need for adding contactors to the existing VVS for Sectors 19 and 20.

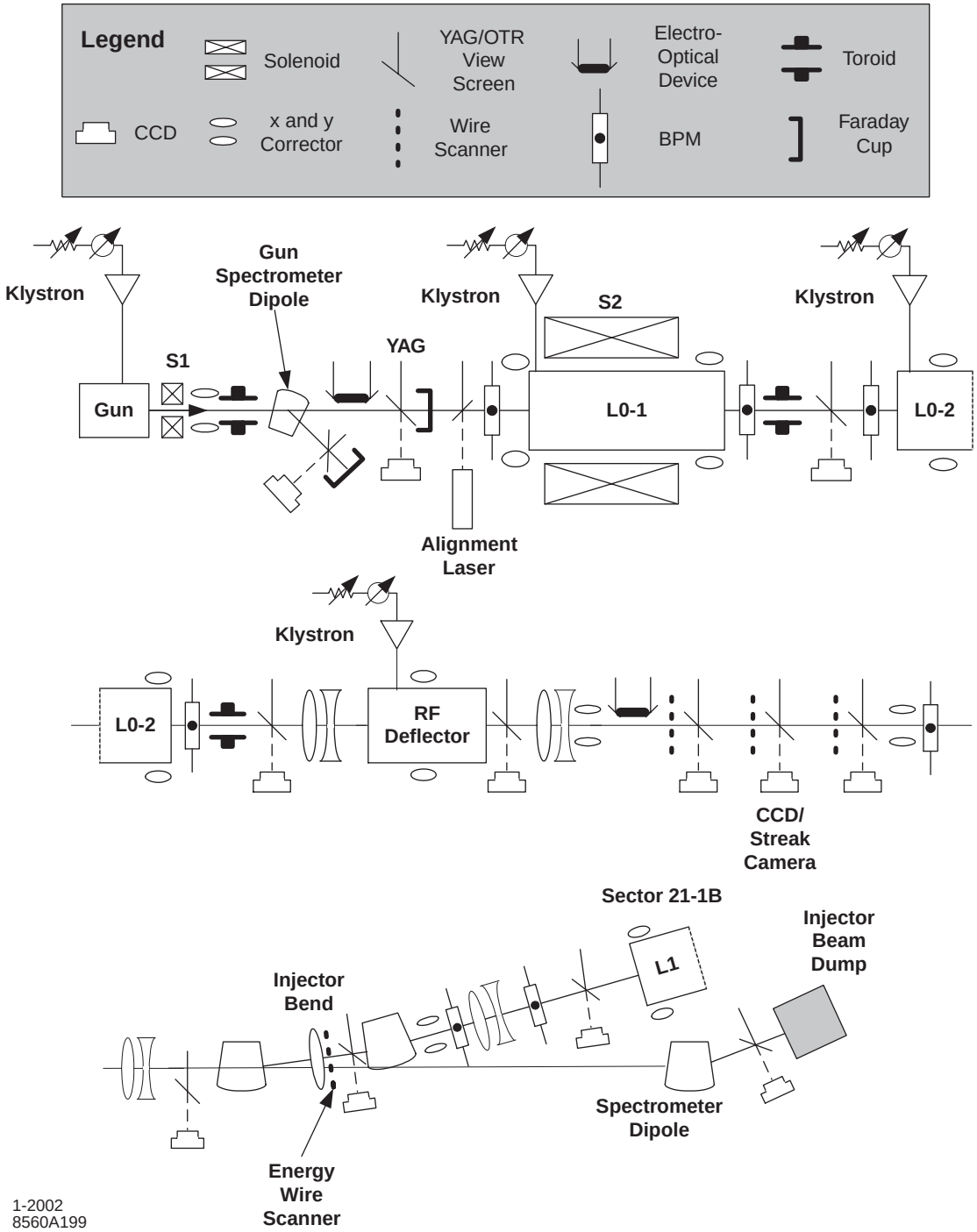

Figure 6.18 Schematic layout (not to scale) showing only the principal beamline elements, the location of diagnostics, and the rf distribution system. Not all BPMs are shown. The Matching Section (MS) begins at the end of the second accelerating section (L0-2). The photoinjector, which includes the MS, ends at the entrance to the Linac 1 (L1).

6.5.2 Standard Beamline Diagnostic Devices

This section discusses diagnostic devices along the injector section of the beamline. The discussion follows the beam from low to high energy, and describes the key measurements to be made in the drifts spaces between accelerating structures. The devices are shown in **Figure 6.18**, which is schematic and has no consistent scale. For a scaled perspective of the space and distances discussed below, refer to **Figure 6.17.**

The photocathode gun is followed immediately by the gun solenoid S1. There is an approximate one-meter drift space between S1 and the linac section L0-1. The diagnostics in this area monitor gun performance and characterize the electron bunch launched from the photocathode. Bunch charge is measured with a toroid, and an electro-optic (EO) device measures the charge distribution in the time domain. (The EO device, an advanced diagnostic, is the topic of **Section 6.5.4,** *Temporal Pulse Shape*.) The charge distribution projected on the plane transverse to beam propagation is observed by inserting a YAG screen into the beam path and imaging the resultant optical profile with a CCD camera. A Faraday cup integrated into the design of the retractable screen allows a simultaneous measurement of bunch charge. Beam energy and energy spread are measured with a dipole spectrometer, which deflects the beam to a low-energy dump. The spectrometer is an important diagnostic for establishing proper rf gun performance and tuning. Transport devices in this section of the beamline include steering coils and BPMs. An alignment laser is used to establish a reference line for view screens along the downstream injector beamline.

The drift space between linac sections L0-1 and L0-2 is one-meter long. A toroid measures charge, and a view screen is available for observing the transverse profile of the bunch. Beam position monitors and steering coils at the exit/entrance of the linac sections are used for beam alignment.

The diagnostic and transport elements in the Matching Section, which begins at the exit of the L0-2 linac, are used to match the 150 MeV injector beam through the bend and into the main linac, starting with L1. A properly matched beam has constraints on its transverse and longitudinal phase-space distributions. The transverse beam parameters, including the emittance, are obtained from beam profiles on the three upstream wire scanners. The wire scanner in the injector bend measures energy spread. The field strengths of the quadrupoles and the placement of the wire scanners are optimized for these measurements, which can be performed during normal beam operations. The longitudinal emittance and its more complicated ΔE-Δt phase-space distribution are determined using the rf deflector cavity, which imparts a time-dependent, vertical kick to the beam. After an extended drift, an image of the beam in the injector bend using the wire scanner or view screen, or alternatively in the injector dump line (see below) using the view screen, gives a direct representation of the longitudinal phase space density (energy and time on perpendicular axes). This information is key to optimizing the injector and understanding the performance of the downstream compressors.

The Matching Section ends at the main linac section L1. The photoinjector can be operated independently of the main linac by turning off the injector bend and delivering the beam to the injector dump. This dump will be used when commissioning the injector, and for troubleshooting and injector studies. A spectrometer dipole on this alternative beam path allows full longitudinal beam analysis when running in this mode.

The rf deflecter allows the longitudinal and horizontal phase space, including the slice energy spread and slice horizontal emittance, to be measured at 150 MeV. See **Section 7.8.2**, *Bunch Length Diagnostics*. Because of their important effect on FEL performance, emittance and energy spread are also measured at several other locations along the path to the undulator. See **Section 7.8.1,** *Tranverse Emittance Diagnostics***,** and **Section 7.8.3**, *Beam Energy Spread Diagnostics*, for further discussion.

Figure 6.18 also shows an electro-optic device and a streak camera in the Matching Section. These devices measure the temporal dependence of the charge distribution within the bunch. Slice emittance and EO diagnostics are the topics of the subsections that follow.

6.5.2 Slice Emittance

The wire-scanners described in **Section 7.8.1**, *Transverse Emittance Diagnostics*, are used to measure the projected transverse emittance of the full electron bunch. However, it is primarily the so-called "slice emittance," the (transverse) emittance of electrons in axial slices that are only a fraction of the full bunch length, that determines the performance of a SASE FEL. The slice scale of interest for a SASE FEL is the slippage length in the undulator, which for the LCLS is 0.5 μm or $1/150^{th}$ of the FWHM length of the compressed bunch at the end of the linac. The length of an equivalent slice at the injector is about 100 fs. Multi-particle simulations of photoinjector beams indicate that within the bunch, the axial variation in the transverse space charge force causes a smooth, non-filamented dilution in phase space density, with concomitant full-bunch emittance growth relative to slice values [7]. The injector diagnostics will only be capable of measuring emittances for slices with lengths on the order of a couple picoseconds. Strategies for minimizing or reversing in the final beam the correlated emittance growth have received considerable attention, as in **Section 6.1.2**, *Emittance Compensation*

Two methods to measure the slice emittance will be available in the MS: one uses the rf deflector, the other a streak camera. As mentioned in **Section 6.5.2**, *Standard Beamline Diagnostic Devices*, the horizontal slice emittance can be measured using the rf deflector in combination with the well-established quadrupole scan procedure and straight-ahead wire scanner or view screen.

As demonstrated at LANL [17], a streak camera can be used in combination with a quadrupole scan to measure the slice emittance if the electron beam is sufficiently intense. A quad scan relies on a set of beamwidth measurements obtained as a quadrupole lens is scanned through a range of focal lengths, and yields the three parameters that characterize the region in phase space occupied by the beam. In a typical application, optical radiation emitted from a screen inserted in the beam path is imaged onto a light sensitive detector, and a beam width

measurement is derived from the spatial dependence of the image intensity. Metal screens are typically prompt (subpicosecond) emitters of optical transition radiation (OTR), making them ideal light sources for preserving the axial structure (intensity) of the incident electron bunch within the emitted optical pulse. An apparatus or procedure capable of resolving both axial and transverse variations in OTR intensity enables a slice emittance measurement. Streak cameras with temporal resolution better than two picoseconds have been available for some time. In a slice emittance application, an image of a line segment on the OTR screen is made at the narrow (20 μm) slit entrance to the streak camera. Preserved in the OTR pulse, the streak tube output displays on its horizontal axis the electron beam intensity along this line segment, and on its vertical axis the temporal dependence of this intensity. A charged coupled device (CCD) image of tube output is ideal for analyzing the beamwidth of different slices, which are represented by some number of adjacent pixel rows.

The feasibility of using a streak camera and OTR optical system as shown in **Figure 6.18** as a backup for the rf deflector to measure the slice emittance at 150 MeV is being studied.

6.5.3 Temporal Pulse Shape

Features of the photoinjector laser system described in **Section 6.4**, *Laser System*, that tailor it for reliable electron production also facilitate applications of the laser to novel electron beam diagnostics. Stable, unconverted laser light (infrared and visible) constitutes a diagnostic beam (probe) for applying electro-optic sampling techniques to the measurement of the temporal shape of the electron bunch. Temporal resolution of sampling measurements is determined by the duration of the probe pulse and its timing jitter relative to the UV pulse (which is used for photoelectron production). Nanosecond delay times can be set with subpicosecond stability for picosecond probe pulses. Probe pulses of millijoule energy are available.

The positive uniaxial crystals $LiNbO_3$ and $LiTaO_3$ are suitable candidates for electro-optic beam sampling. In the linear or Pockels regime, bias fields generated by the electron beam do not alter the crystal anisotropy. In previous work with 16-MeV electrons, wakefield-induced phase retardation in $LiTaO_3$ has been demonstrated with resolution of order 10^{-1} radians with wakefield sensitivity of order 1 radian-m/MV [50]. More recent work has demonstrated single-shot bunch shape measurements using a wavelength-chirped laser pulse [51].

The electron beam longitudinal distribution and bunch length will be monitored noninvasively using beam wakefield components as a Pockels-effect bias to induce accumulated phase retardation of a probe pulse as it propagates through the crystal. The wakefield-induced Pockels effect generates a linear response that is determined by wakefield dynamics. In a standard configuration using cross-polarized optics, a null signal is set for zero wakefield amplitude; i.e., when the probe waveform and beam wakefield are not coincident. Incident and transmitted probe pulses are transported to and from the crystal location by polarization-preserving optical fiber. In general, picosecond or nanosecond (i.e., uncompressed) probe durations can be used. In the picosecond case, signals can be scanned by varying the relative probe-beam timing. This

scanning may not be necessary for the nanosecond case if a fast detector is available as discussed next.

Coincidence of the probe and beam wakefield timing generates a transmitted probe signal proportional to its accumulated retardation phase. This signal can be detected with fast diodes (tens of gigahertz bandwidths) and transient digitizers, or a streak camera, as well as with frequency-resolved optical-gating (FROG) [48]. FROG is an established ultrafast diagnostic, which measures the amplitude and phase history of the transmitted probe waveform with subpicosecond resolution. It is best suited for signals of short (picosecond) and ultrashort (subpicosecond) duration. Known electro-optic coefficients can also be used to estimate wakefield amplitudes from the probe signal.

The noninvasive feature of this diagnostic method affords the use of multiple sampling sites of known spacing for improved measurement of electron beam effects.

6.6 PARMELA Simulations

6.6.1 Initial Conditions

Emittance growth in the photoinjector from the rf gun through Linac 0 and the Matching Section has been studied using simulations based primarily on Version 3 of the LANL-maintained code PARMELA. The electric field map of the gun was obtained with SUPERFISH and directly used in PARMELA. SUPERFISH was also used to simulate the fields in the traveling-wave accelerating sections, and space harmonics were calculated for use in PARMELA. RF fields were assumed to be cylindrically symmetric. This is a reasonable assumption since, as discussed in **Section 6.3.3**, *Symmetrization*, the dipole rf fields which are normally dominant in an rf gun have been largely eliminated in the prototype gun [10]. Using a 3D map of fields generated with MAFIA, the UCLA version of PARMELA was used to verify that the higher order field components (i.e., quadrupole and higher) make a negligible contribution to the emittance growth in the gun. Work is in progress to study the effect of the dipole field phase component induced by single side rf power flow.

A comparison of PARMELA, both UCLS and LANL versions, with two PIC codes, Magic2D and Maxwell-T, was made to study the representation of image charges on the cathode. The codes agreed to within 20% on the transverse emittances and space-charge field strengths in the first picoseconds after emission. (Interestingly, both PIC codes estimated lower emittances than either version of PARMELA.)

A magnetic field map for the emittance compensating solenoid at the gun was produced using POISSON and passed to PARMELA. The field generated by POISSON is shown in **Figure 6.19**. It can be compared to the measured field shown in **Figure 6.12**. The magnetic field for the air core solenoid around the first accelerating section was modeled in PARMELA using single coils each with appropriate strength to represent the field.

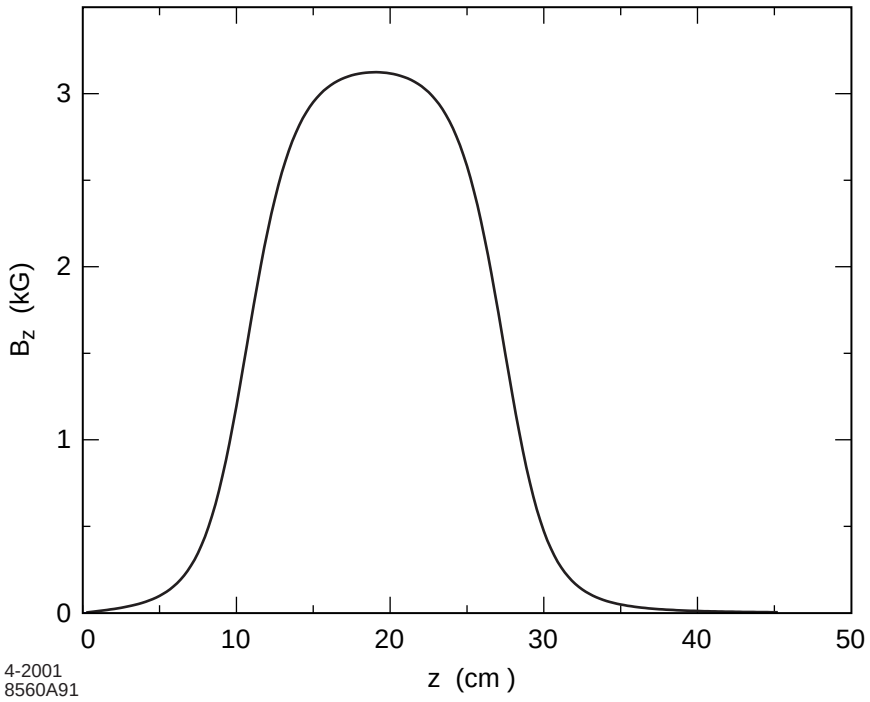

Figure 6.19 Axial magnetic field generated using POISSON of the emittance compensation solenoid as a function of distance *z* along the axis for excitation current of 221 A. The cathode surface is located at z=0 mm.

The multi-parameter space including charge, laser spot size, pulse length, solenoid field and accelerating gradient has been explored for tuning the 1.6-cell S-band rf gun beamline using a variety of simulation codes. (See **Section 6.1.2**, *Emittance Compensation.)* The overall result is that to produce a beam of the highest possible brightness, a 1-mm radius and 10-ps bunch length is about optimum for 1 nC of charge if the peak rf field at the cathode is 140 MV/m. Nearly identical results can be obtained using 120 MV/m if the radius is increased to 1.2 mm. It is also clear that using spatial and temporal distributions that are uniform (flat top) rather than Gaussian will improve the resulting transverse emittance. As a practical matter, uniform temporal distributions can only be approximated. Therefore the PARMELA simulations discussed here have usually assumed rise times of 0.35 ps or 0.7 ps, which are within the capability of the laser system described in **Section 6.4**, *Laser System*. For the PARMELA simulations, the initial temporal uniform distribution was generated by stacking 9(17) Gaussian distributions with an rms width of 0.35(0.7)º S-band phase, each separated by 0.6(1.1)° of S-band phase. The resulting temporal bunch shape is shown in **Figure 6.20** for a rise time of 0.35 ps and in **Figure 6.21** for 0.7 ps. A uniform spatial distribution is assumed for all the PARMELA simulations.

The basic layout of Linac 0 (L0) and the Matching Section (MS) are shown in **Figure 6.17**. The corresponding input parameters assumed for the PARMELA simulations are summarized in **Table 6.4**. A first series of simulations was done at 140 MV/m and injection phase of 32° and is described in **Section 6.6.2,** *Optimization for 140 MV/m*. However, the initial operation of the gun

is likely to be at 120 MV/m to avoid rf breakdown. An optimization for 120 MV/m is presented in **Section 6.6.3**, *Optimization for 120 MV/m*.

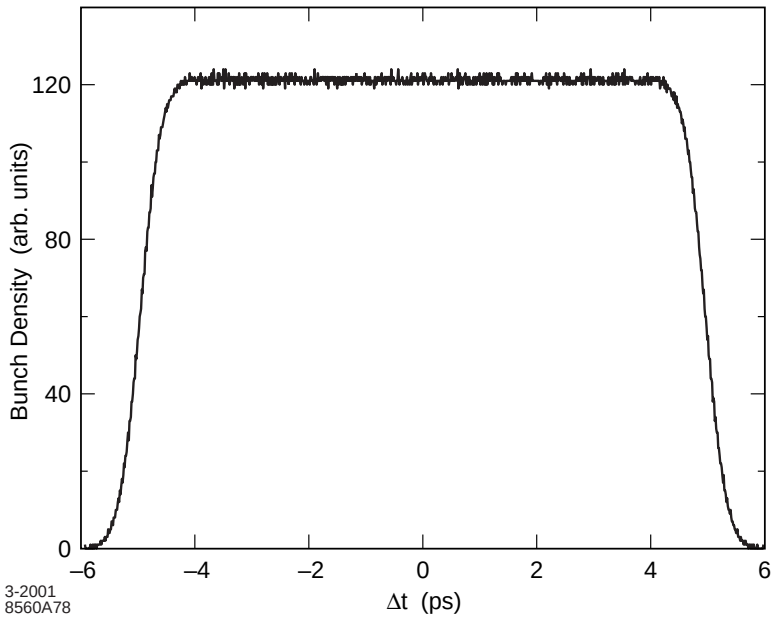

Figure 6.20 Temporal shape of electron pulse used as input for PARMELA simulations for the rf photoinjector. The rise time is about 0.35 ps.

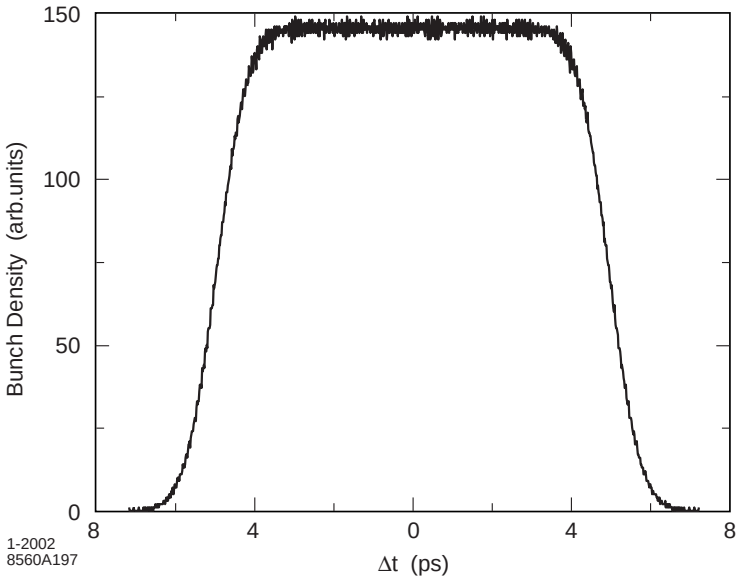

Figure 6.21 Temporal shape of electron pulse used as input for PARMELA simulations for the rf photoinjector. The rise time is about 0.7 ps.

Table 6.4 Input Parameters for PARMELA Simulation.

Parameter	Value at 140 MV/m	Value at 120 MV/m
Bunch charge at cathode	1.0 nC	1.0 nC
Longitudinal charge distribution at cathode	Uniform, rise time 0.35 and 0.7 ps	Uniform, rise time 0.35 and 0.7 ps
Transverse charge distr. at cathode	Uniform	Uniform
Bunch length at cathode	2.9 ps rms	2.9 ps rms
Bunch radius at cathode	1 mm hard edge	1.2 mm hard edge
Peak rf field at cathode	140 MV/m	120 MV/m
Injection phase	32º	27.3º
Emittance compensating solenoid:		
Axial field	3.15 kG	2.71 kG
Physical length	22.5 cm	22.5 cm
Location[a] of peak field (also center of physical solenoid)	19.1 cm	19.1 cm
Booster accelerator:		
Accelerating gradient L0-1	24.1 MV/m	18 MV/m
Location[a] of input coupler for first Section	1.4 m	1.41 m
Accelerating gradient L0-2	24.1 MV/m	30.5 MV/m
Linac focusing solenoid:		
Axial field	-1.75 kG	-0.75 kG
Physical length	1.0 m	0.80 m
Location[a] of start of physical solenoid	1.43 m	1.40 m
Location[a] of exit of L0	7.9 m	8.4 m
Thermal emittance, $\varepsilon_{n,th}$	0.3/ 0.5μm rms	0.3/0.5 μm rms

a With respect to position of cathode.

The emittance compensating solenoid is physically 22.5 cm long. For the simulations it is placed against the downstream edge of the rf gun, which results in the center of the solenoidal field being 19.1 cm from the cathode surface. The field map (**Figure 6.19**) indicates that for this configuration the field at the cathode is essentially zero without the use of a bucking coil.

6.6.2 Optimization for 140 MV/m

Using only the gun, solenoid, and the immediately following drift space (i.e., no booster), a minimum value for the first emittance minimum along the drift was obtained by varying the solenoidal field and beam spot radius. A value of B_z = 3.15 kG and hard-edge radius of 1 mm was found to be optimum. The emittance minimum very nearly coincides with that of the new working point described in **Section 6.1.3**, *Design Principles*. The slightly larger value of B_Z here is consistent with the solenoid being displaced somewhat downstream because of the physical interference with the gun structure.

Next, including both the boosters (with an accelerating gradient of 24.1 MV/m) and the second solenoid (S2), the emittance at the booster exit was minimized by varying the booster locations (keeping the drift distance between the two sections fixed at 0.5 m. The results are summarized in **Figure 6.22**, which is really a compilation of 12 independent figures. The optimum position of the entrance to the first section was found to be 1.4 m from the cathode (the S2 field was -1.5 kG). Note that as the booster is moved toward the position for the minimum emittance, the emittance decreases more gently and eventually monotonically, approximating the shape shown in **Figure 6.3**. Finally the emittance was minimized by varying the field and position of S2. An emittance minimum was found for a field of -1.75 kG and by positioning the start of the solenoid at 1.43 m with respect to the cathode. Finally, a thermal emittance of 0.3 μm was added to the PARMELA deck [8]. Using these parameters and an input pulse rise time of 0.35 ps, a final emittance of 0.8 μm was obtained for a 20 K-particle run. See **Figure 6.23**. Using the same parameters but substituting a rise time of 0.7 ps for the input pulse increased the emittance by about 10%.

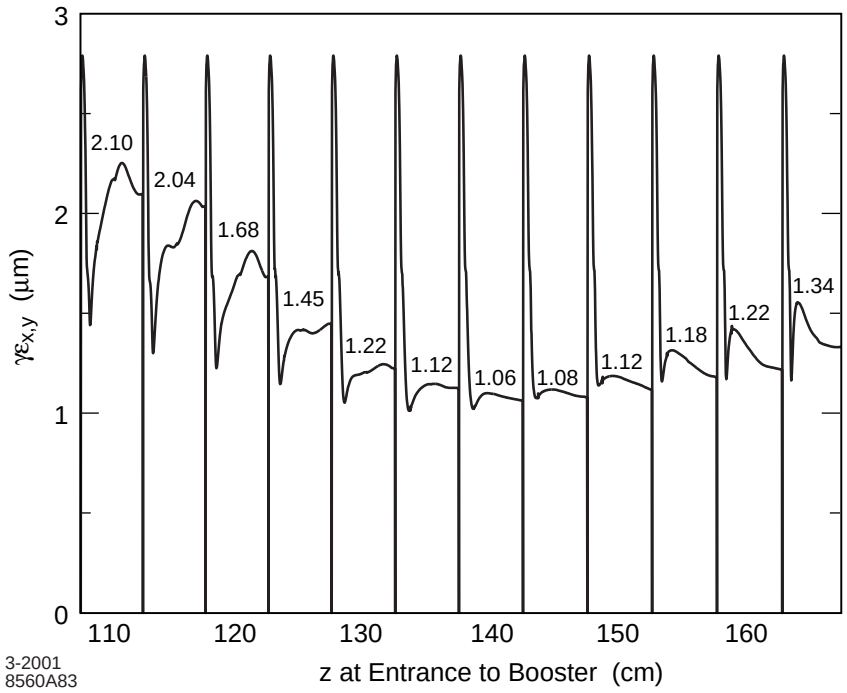

Figure 6.22 Emittance as a function of distance between cathode and booster-entrance is shown for 12 different positions of the booster. The minimum emittance at the booster-exit is indicated for each position. In each case the emittance compensating solenoid is set to B_z=3.15 kG.

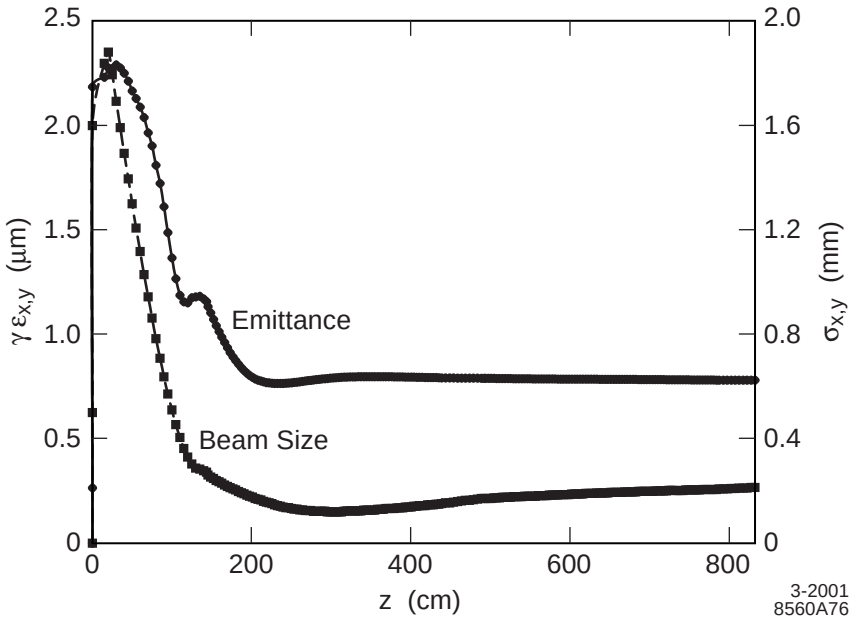

Figure 6.23 Transverse normalized rms emittance as a function of distance from the cathode for 20 K particles. A rise time of 0.35 ps is assumed. A normalized rms thermal emittance of 0.3 μm is included.

The PARMELA simulation results are summarized in **Table 6.5**. As indicated therein, there is no significant improvement in the emittance generated by PARMELA as the number of particles tracked is increased beyond 20 K. However, as needed by the algorithm computing the space charge for a 3D geometry, the number of particles was increased to 100K to study the evolution of the beam in the Matching Section within which the beam becomes elliptical. The normalized transverse phase space at the exit of L0 for 100K particles is shown in **Figure 6.24**. The upper left plot is a normalized *x*-*y* scatter plot, with x_n and y_n amplitudes in units of rms beam size. The normalized $x_n - x'_n$ phase space is shown in the upper right with the rms emittance ellipse given by the circle of unity radius in the center. The normalized rms slice emittance in *x* and *y*, as a function of axial distance along the bunch, is shown in the lower left. The projected value is shown by the horizontal dotted line. In the lower right, the beta-mismatch amplitude, ζ, is shown as a function of Δz. The beta-mismatch amplitude between the slice Twiss parameters and the projected Twiss parameters is defined by **Eq. (7.26)** in **Section 7.6.1**, *Electron Beam Evaluation*. The mismatch is normalized such that $\zeta \geq 1$. A large variation in ζ within the bunch, which persists through the linac, may degrade the final FEL gain.

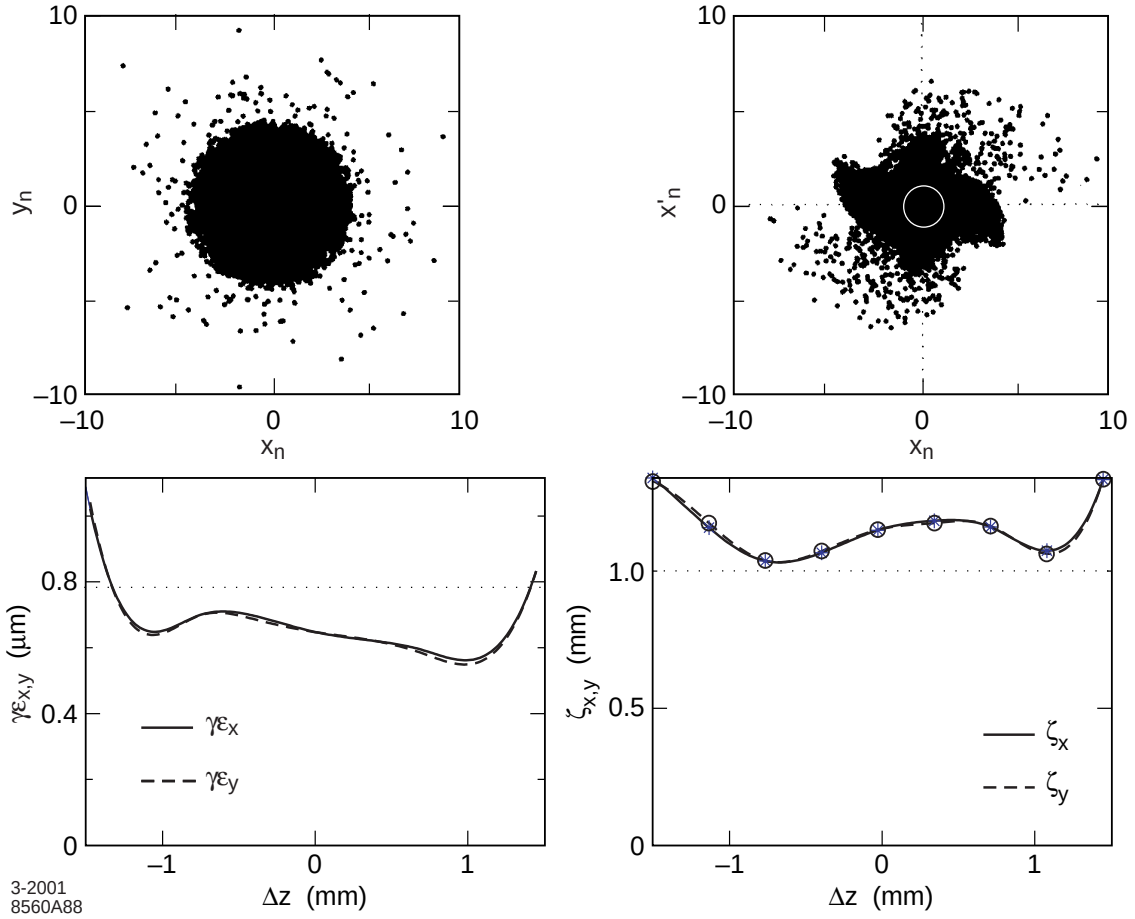

Figure 6.24 Normalized transverse phase space at the exit of L0 for 100K particles. (1) Distribution of particles in the beam (upper plots). The scales are derived from the right-hand figure in which the rms emittance ellipse in the x-x' plane (only) is normalized to a circle having a radius of unity. (2) Transverse normalized slice emittances (lower left plot) in both planes and mismatch parameter, ζ, (lower right plot) in both planes along the bunch z-axis. In this figure, the bunch head is at the left, as in the convention of Chapter 7, Accelerator.

The phase space plots for a series of 9 slices identified in the lower right plot of **Figure 6.24** are displayed in **Figure 6.25**. The blue/dark background in each case is the full projection in the x-x' plane, identical to the upper right plot of **Figure 6.24**. The red/light area represents the distribution in the x-x' plane of the particles in the particular slice. Note that the "halo" (particles outside the main core) occurs primarily in the first (head) and last (tail) slices.

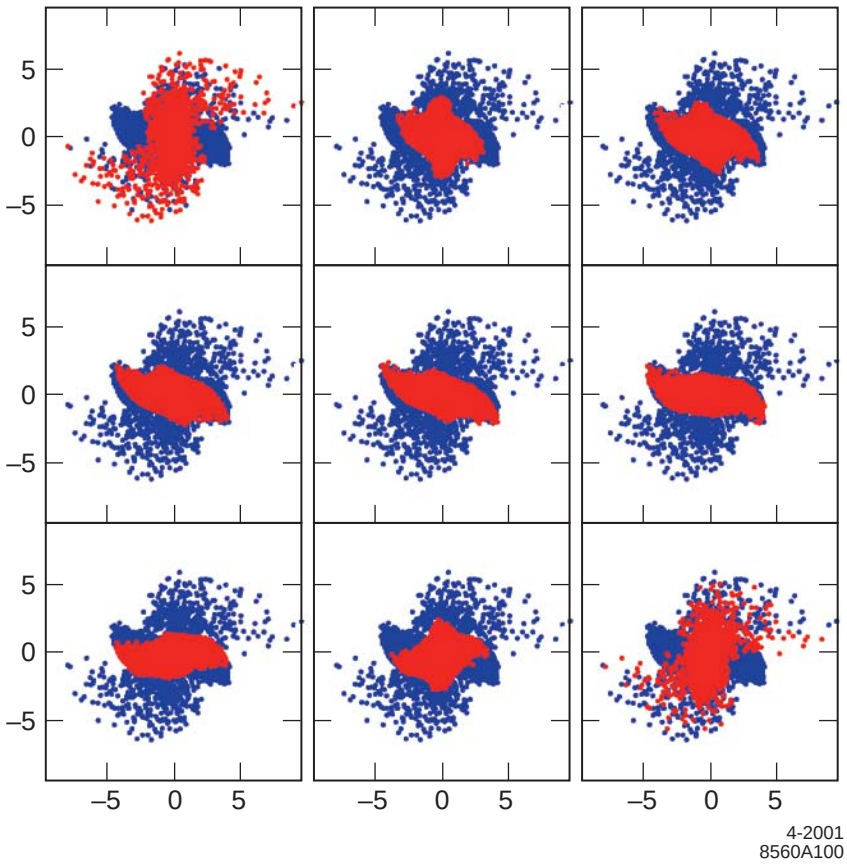

Figure 6.25 Transverse distribution in the x-x' plane of particles in a slice (red/light) at the exit of L0 for 100K particles shown against a background of the full projection (blue/dark). Scales are the same as for the upper right plot of **Figure 6.24.** In each plot read left to right, the location of the slice along the z-axis of the bunch can be identified by the corresponding asterisk in the lower right plot of **Figure 6.24**.

The longitudinal distribution of particles at the exit of L0 is shown in **Figure 6.26**. The energy as a function of axial position within the bunch is shown in the upper left with the corresponding particle distributions projected out from both planes shown in the upper right and lower left. The lower right distribution is the same as the lower left, but in terms of peak current instead of number of particles, and time instead of axial position.

The rms energy spread of the distribution shown in the upper right of **Figure 6.26** is $\sigma_\gamma / \gamma_o = 0.18\%$. The L0-2 phase is set such that when the wakefields are included the total energy spread will be minimized. The effects of longitudinal wakefields in the booster are calculated using the 2D simulation code LiTrack (see **Section 7.2.5**, *2D Tracking Studies*) with the PARMELA results at the exit of L0 as input. The rms energy spread in this case is reduced to 0.1%. As indicated in **Section 6.1.1**, *Beam Requirements*, a low value of slice energy spread is also desired. The slice energy spread is plotted as a function of axial position in **Figure 6.27**. It can be seen that for the core of the distribution the slice energy spread is $\sigma_\gamma^{slice} / \gamma_o < 0.005\%$.

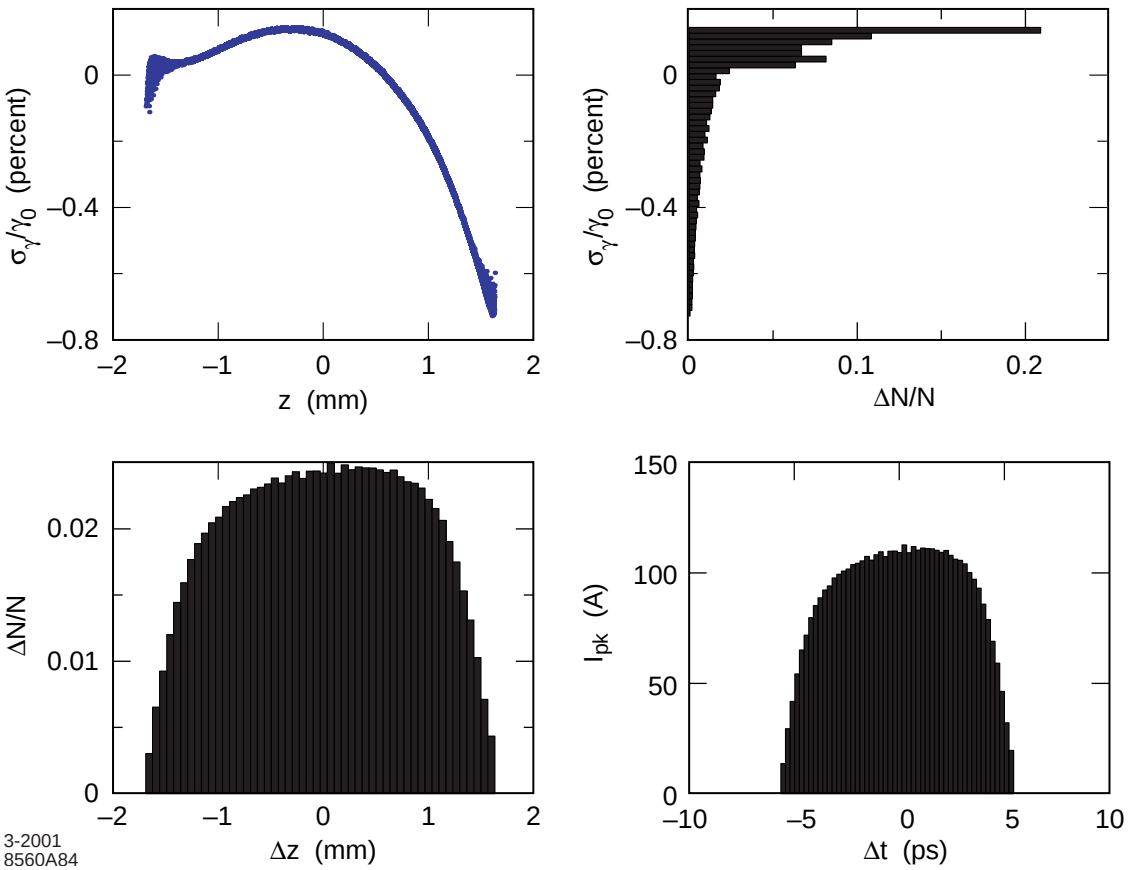

Figure 6.26 Longitudinal distribution of particles in the beam at the exit of L0 for 100 K particles. In this figure, the bunch head is at the left, as in the convention of **Chapter 7**, *Accelerator*.

The Matching Section between L0 and L1 was designed using the simulation code MAD. A plot of the TWISS parameters as a function of axial distance along the beamline is shown in **Figure 7.33**. It is seen from the figure that the beta function gets very small, which could potentially result in undesirable emittance growth due to the high space charge density at this relatively low energy. To check for this possibility, the PARMELA simulation was extended through the MS. Since the beam size aspect ratio reaches 12, cylindrical symmetry cannot be assumed. The 100 K particle distribution shown in **Figs. 6.24** to **26** was launched into the MS using Version 3 of PARMELA. The resulting particle distribution at the end of the MS (i.e., at the beginning of L1) is shown in **Figs. 6.28** and **29** for. Note that although some small asymmetry between the x- and y-emittances creeps in, there is no significant emittance growth.

The emittance values derived from the full distribution of particles are strongly influenced by the few particles outside the core. In **Figure 6.30**, the slice emittance along the bunch is displayed for various cuts in the transverse tails. A 5% cut in the tails reduces the emittance for the central slices by about 15%. The effect is even more dramatic when the brightness of each slice is plotted, as in **Figure 6.31**.

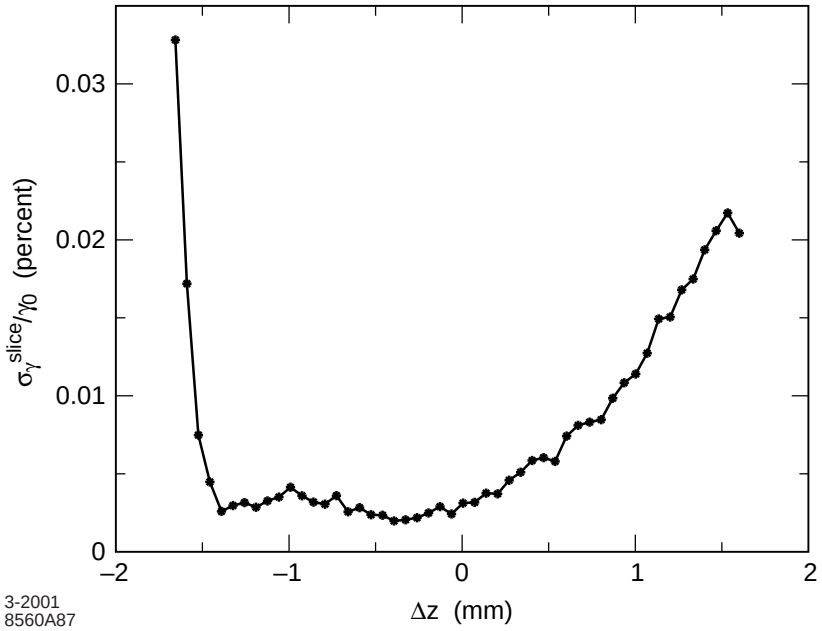

Figure 6.27 Slice energy spread at the exit of L0 as a function of axial position. In this figure, the bunch head is at the left, as in the convention of **Chapter 7**, *Accelerator*.

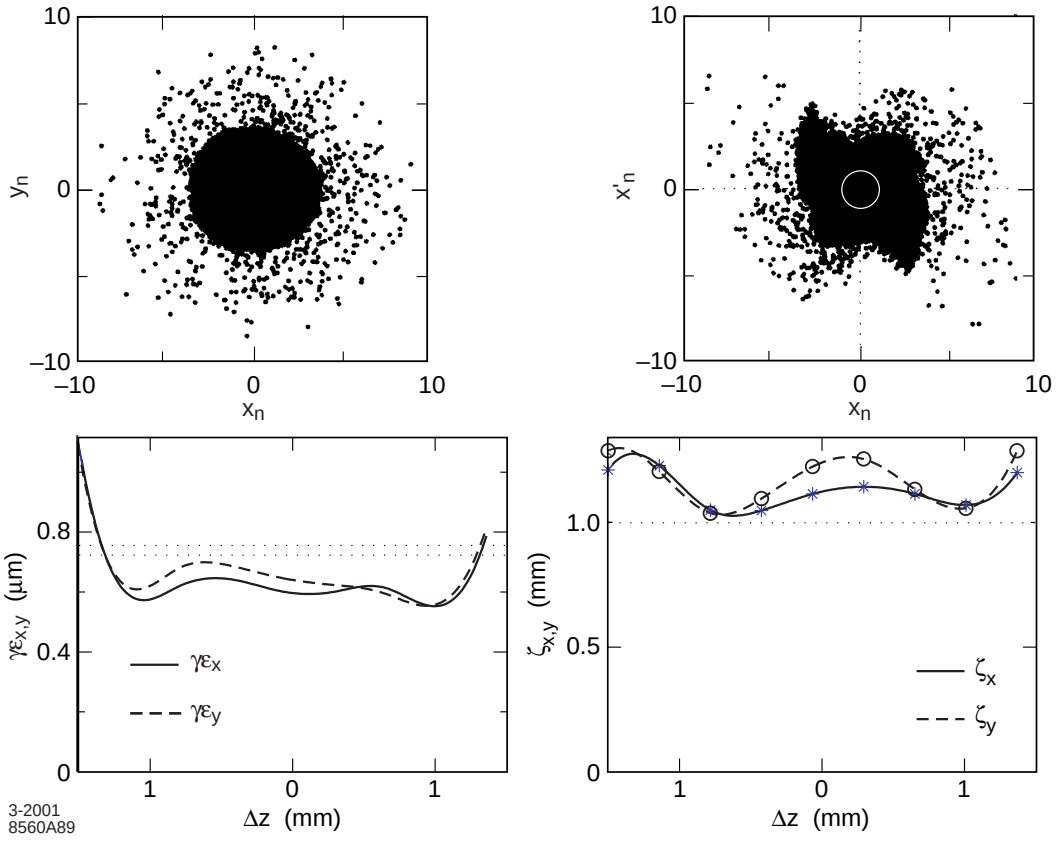

Figure 6.28 Transverse distribution of particles in the beam at the exit of MS. In this figure, the bunch head is at the left, as in the convention of **Chapter 7**, *Accelerator*.

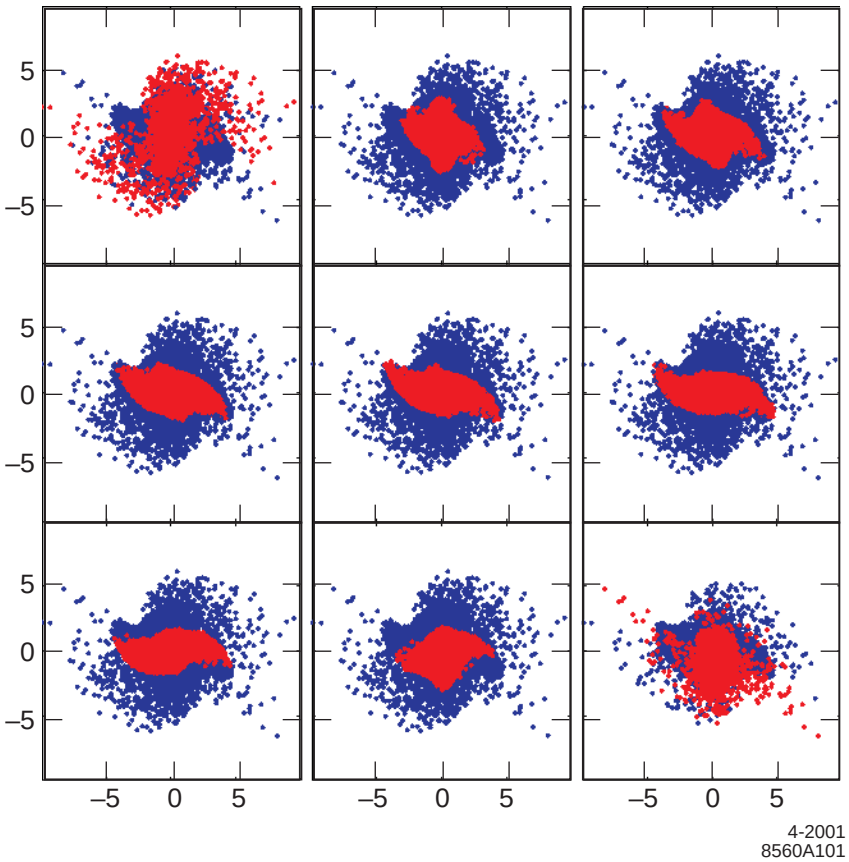

Figure 6.29 Slice emittance at the exit of MS.

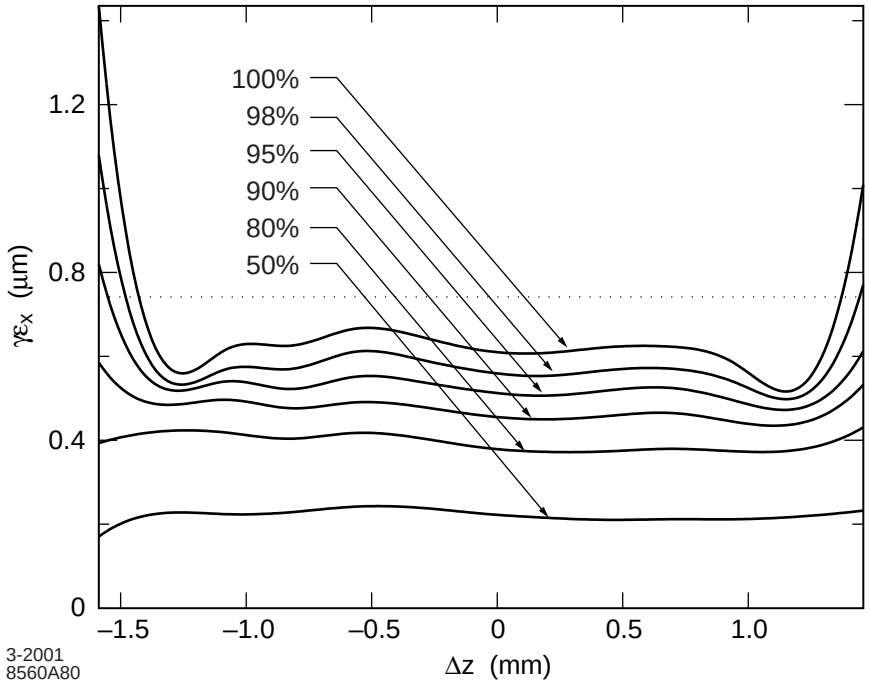

Figure 6.30 Slice emittance along bunch at end of MS for different cuts of transverse dimension.

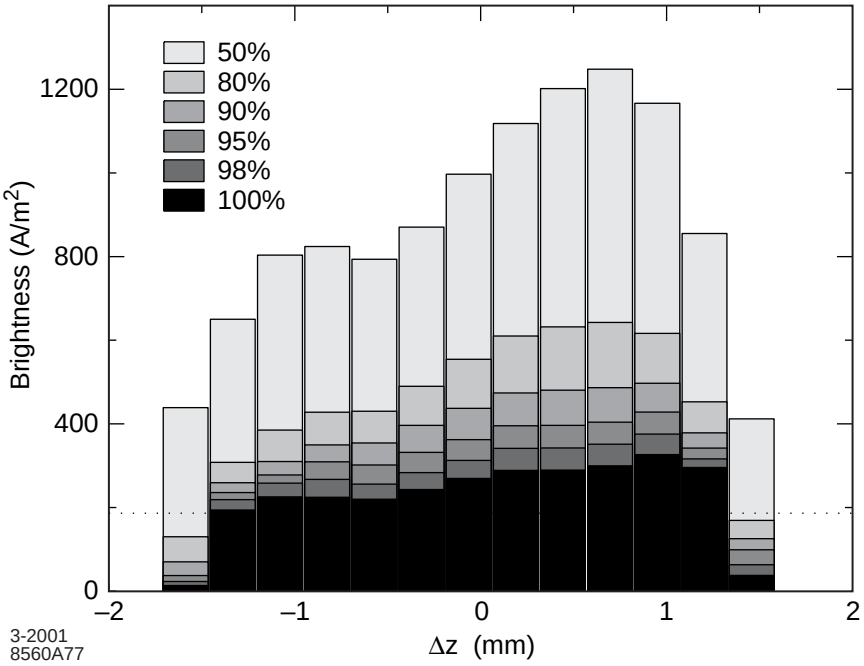

Figure 6.31 Brightness along bunch at end of MS for different cuts of transverse distribution.

Comparing the PARMELA output values shown here with the required values given in **Table 6.1**, it is seen that the emittance is comfortably below the required value. The variation of emittance with increase in rise time, decrease in number of particles tracked, and the effect of excluding thermal emittance are indicated. The energy spread—both projected and slice—are also within requirements. However, according to preliminary measurements performed at the Gun Test Facility (GTF), the correlated energy at the exit of the gun would be underestimated in the PARMELA simulations. Analytical work and PIC code simulations are in progress. While the rms bunch length doesn't change in either the L0 or MS, the temporal bunch shape becomes somewhat less uniform. Nonetheless, an examination of **Figure 6.26,** shows that for over about 65% of the bunch length the peak current is >100 A.

Table 6.5 PARMELA Output Parameters.

Parameter	Value
Bunch charge	1.0 nC
Booster phase	2°
Bunch length	2.9 ps rms
Energy	150 MeV
Integrated energy spread, σ_γ / γ_0	0.10% rms
Slice energy spread, $\sigma_\gamma^{slice} / \gamma_0$	0.005% rms
Emittance at 20 cm from exit of L0-2 for 0.7 ps rise time; below e_{th} in μm/no. particles tracked:	**$\varepsilon_{n,rms}$ (μm); below for 140/120 MV/m:**
0.3/10 K	0.926/0.929
0.5/10 K	0.952/0.956
0.3/100 K	0.922/
0.3/200 K	/0.919
0.5/100 K	0.948/
0.5/200 K	/0.958
Emittance at 20 cm from exit of L0-2 for 0.35 ps rise time; below e_{th} in μm/no. particles tracked:	**$\varepsilon_{n,rms}$ (μm); below for 140MV/m / 120MV/m:**
0.3/20 K	0.80/
0.3/100 K	0.78/ 0.80

6.6.3 Optimization for 120 MV/m

Typically S-band rf guns operate with peak rf fields of 120 MV/m or lower. Higher fields usually lead to excessive dark current or frequent rf breakdowns. Although a great deal of care will be taken to construct the LCLS gun so as to avoid these problems (the load-lock should help as well), the initial gun operation is anticipated to be at about 120 MV/m. In this section, a reoptimization of the injector parameters is made for the case of 120 MV/m in order to determine more exactly the emittance achievable during initial operation.

First HOMDYN was used to explore the transverse parameter space for a square pulse of 10 ps. The parameters that were examined included the gun solenoid (S1) field value, the injection phase, the linac position and gradient and the second solenoid (S2) field value. For a thermal emittance of 0.5 μm, the minimum normalized transverse emittance obtained was 0.6 μm rms using an injection phase of 20°, S1 field of 2.71 kG, and a linac field of 24 MV/m (33 MV/m in HOMDYN units) with the entrance to L0-1 located 1.4 m from the cathode.

When the same parameters were used in PARMELA, including a square pulse of 10 ps, an emittance of 0.99 μm was obtained. The higher emittance with PARMELA confirms that the parameter space near the working point as determined with HOMDYN must be further optimized with PARMELA. The parameter space was explored using PARMELA for a pulse with a finite rise time of 0.7 ps. (HOMDYN uses only absolutely square pulses.) The PARMELA optimization was initiated with parameter values obtained from the optimization with HOMDYN. The initial pulse profile is shown in **Figure 6.21**. It is built with 9 Gaussians of width 0.7 ps rms separated by 1.1 ps.

A first series of simulations was performed with a spot-size radius of 1 mm. The best emittance was obtained by placing L0-1 2.2 m away from the cathode. This solution was unsatisfactory as the same linac section is located 1.42 m from the cathode when parameters are optimized with the cathode peak rf field at 140 MV/m.

To keep the distance cathode-to-Linac constant, the spot radius was increased from 1 mm to 1.2 mm. This larger radius reduces the space charge effect without introducing excessive additional RF defocusing effects. Also, the field in L0-1 was decreased from 24.1 MV/m to 18 MV/m following the criteria presented in **Eq. 6.3**. This results in an energy at the exit of L0-1 of 58.25 MeV instead of 78.18 MeV . By running L0-2 at 24.1 MV/m and 30.5 MV/m, the energy at the end of the beamline is 130 MeV and 150 MeV respectively. No emittance growth in the Matching Section appears for either a 130 MeV or 150 MeV beam.

With the parameters presented in **Table 6.4** for 10 K particles and 0.7 ps rise time, the beam is smoothly converging along the beamline as presented in **Figure 6.32**. The projected emittance is 0.93 μm.

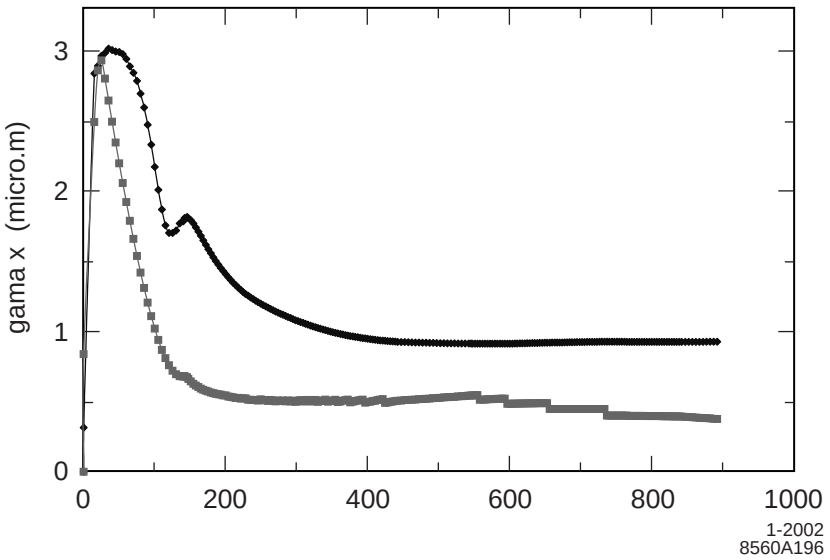

Figure 6.32 Transverse normalized rms emittance as a function of distance from the cathode for 10K particles. A rise time of 0.7 ps is assumed. A normalized rms thermal emittance of 0.3 μm is included.

Figure 6.33 shows the transverse profile, horizontal phase space, slice emittance and mismatch parameters for 9 slices at the end of L0-2. When the bunch is cut into 99 slices, 97% of the particles are contained in slices, which have an emittance smaller than 1 mm.mrad, while 71% of the particles are contained in slices, which have an emittance smaller than 0.8 μm. By choosing to use 99 slices, each slice when transported to the undulator will have a length comparable to a slippage length. **Figure 6.34** shows the longitudinal phase space distribution (upper left) and the projections on the upper right (energy) and lower left (time) at the end of L0-2. The L0-2 phase was chosen to minimize energy spread after including wakefield effects. Before including the wakefields the rms energy spread was 0.2% and after the inclusion of wakefields it became 0.06%.

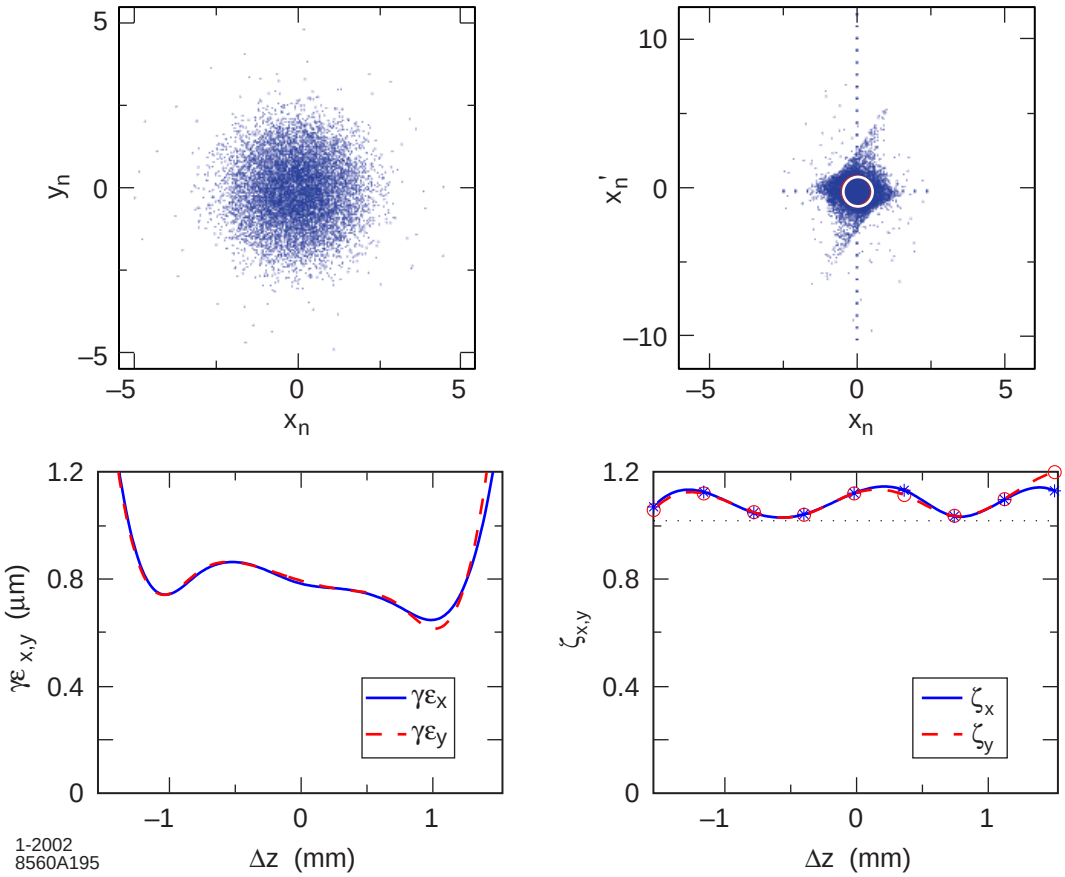

Figure 6.33 Longitudinal distribution of particles in the beam at the exit of L0-2. In this figure, the bunch head is at the left, as in the convention of **Chapter 7**, *Accelerator*. The peak rf field at the cathode is 120 MV/m.

The optimization of the beamline for the gun run at 120 MV/m gives a projected emittance very similar to that obtained when optimizing the beamline for the gun run at 140 MV/m. See **Table 6.5**. Similarly, for a rise time for the 10 ps pulse of 0.7 ps, a projected emittance as small as 0.8 μm has been computed with the gun run at 120 MV/m.

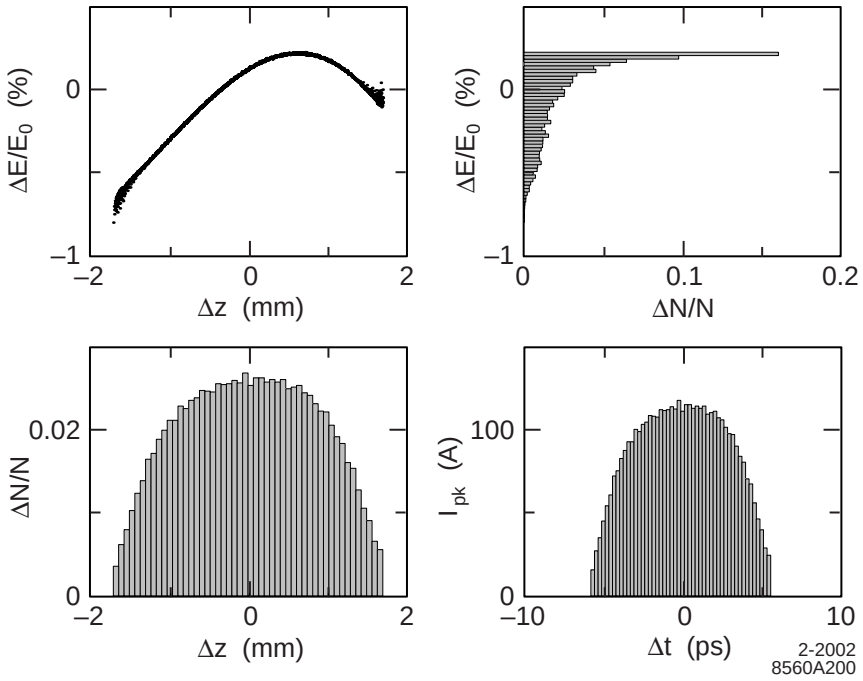

Figure 6.34 Longitudinal distribution of particles in the beam at the exit of L0-2. In this figure, the bunch head is at the left, as in the convention of **Chapter 7**, *Accelerator*. The peak rf field at the cathode is 120 MV/m.

6.6.4 Sensitivity Study

To define levels of regulation on power supplies for the RF power feed and for the emittance compensation solenoid, and to specify requirements on the UV laser pulse stability and reproducibility, a sensitivity study was performed on the beamline optimized for a peak rf field at the cathode of 120 MV/m. A single parameter was changed around its nominal value. The evolution of the emittance at the end of Linac 0-2 (L0-2) as a function of this parameter is shown in the 6 plots of **Figure 6.35**. To keep the projected emittance below 1 μm, the peak RF field amplitude should not vary by more than 0.5 MV/m around 120 MV/m, the balance of the fields between the half cell and the full cell should not vary by more than 1% (ongoing studies indicate that 3% is probably more correct), and the laser injection phase should not vary by more than 4° S-Band. These are large variations compared to the much tighter tolerances that these systems normally meet. It is noted that a variation of only 0.4% on the solenoid field (S1) value increases the projected emittance from 0.93 to 1 μm. However, a tolerance of 0.1% or better will not difficult to achieve with the solenoid power supply.

A variation of ±0.1 mm on the laser spot radius also gives a projected emittance close to 1 μm. Finally an increase of 10% in charge still leaves the projected emittance just below 1 μm.

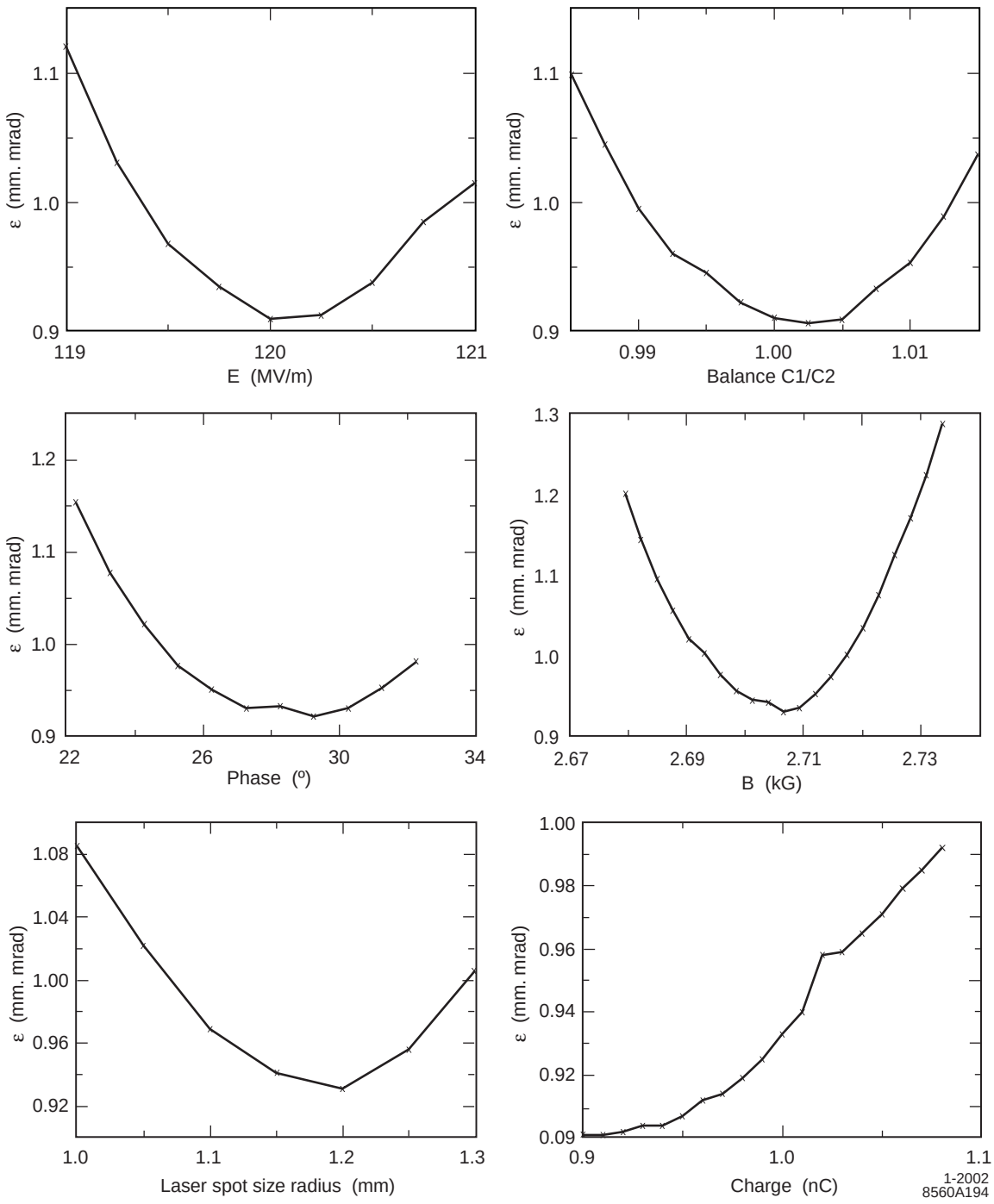

Figure 6.35 Emittance at the end of Linac 0-2 as a function of a single parameter with all other held at the value obtained when all parameters are optimized simultaneously.

The final tolerances on power supplies and on the laser beam properties will be slightly tighter than what is indicated above. All these variations combined together should give a deterioration of emittance such that on average the final projected emittance is on the order of the quadrature sum of the emittances obtained with single parameter variations. A study is underway

to determine the full range of variations to be expected when the variations of each individual parameter are combined.

6.7 References

1 J.F. Schmerge et al., "Photocathode rf gun emittance measurements using variable length laser pulses," in *SPIE 3614* (1999), p. 22.

2 D.T. Palmer et al., "Emittance studies of the BNL/SLAC/UCLA 1.6 cell photocathode rf gun," in *Proc. of the 1997 Particle Accelerator Conf.*, p. 2687.

3 M. Babzien *et al*., "Observation of self-amplified spontaneous emission in the near-infrared and visible," *Phys. Rev. E* 57 (1998) 6093.

4 R. Alley *et al*, "The design for the LCLS rf photoinjector," *Nucl. Instrum. and Meth. A* 429 (1999) 324.

5 J. Rosenzweig and E. Colby, "Charge and wavelength scaling of rf photoinjector designs," in *AIP Conf. Proc. 335* (1995), p. 724.

6 B. E. Carlsten, *Nucl. Instrum. and Meth. A* 285 (1989) 313.

7 L. Serafini and J. B. Rosenzweig, "Envelope analysis of intense relativistic quasilaminar beams in rf photoinjectors: a theory of emittance compensation," *Phys. Rev. E* 55 (1997) 7565.

8 J. Clendenin *et al*., "Reduction of thermal emittance of rf guns," *Nucl. Instrum. and Meth. A* 455 (2000) 198.

9 M. Ferrario, A. Mosnier, L. Serafini, F. Tazzioli and J. M. Tessier, "Multi-bunch energy spread induced by beam loading in a standing wave structure," *Part. Acc*. 52 (1996).

10 D. T. Palmer, "The next generation photoinjector," Ph. D. Thesis, Stanford University (1998).

11 M. Ferrario, J. E. Clendenin, D. T. Palmer, J. B. Rosenzweig and L. Serafini, "HOMDYN study for the LCLS rf photo-injector", in *The Physics of High Brightness Beams*, World Scienific (2000), p. 534.

12 J. Rosenzweig and L. Serafini, "Transverse particle motion in radio-frequency linear accelerators," *Phys. Rev. E* 49 (1994) 1599.

13 D.T. Palmer, S. Anderson and J.B. Rosenzweig, "Single Crystal Copper Photo-Cathode in the BNL/SLAC/UCLA 1.6 Cell RF Gun," in *The Physics of High Brightness Beams*, World Scienific (2000), p. 439.

14 J.F. Schmerge *et al*., "Transverse emittance measurements on an S-band rf gun," *SLAC-PUB-8963* (2001), to be published in Nucl. Intrum. and Meth. A.

15 X.J. Wang et al., *J. Appl. Phys*. 72 (1992) 888.

16 P. G. O'Shea and L. Spentzouris, in *AIP Conf. Proc*. *472* (1999), p. 212.

17 S.M. Gierman, "Streak Camera Enhanced Quadrupole Scan Technique", in *The Physics of High Brightness Beams*, World Scienific (2000), p. 511.

18 W.S. Graves *et al*., "Measurement of thermal emittance for a copper photocathode," in *Proc. of the 2001 Particle Accelerator Conf*., p. 2227.

19 J.E. Clendenin and G.A. Mulhollan, "High quantum yield, low emittance electron sources," in *Quantum Aspects of Beam Physics*, Singapore, World Scientific (1999), p. 254.

20 D.H. Dowell, S. Joly and A. Loulergue, "Space charge limits of longitudinal emittance in RF photoinjectors," in *AIP Conf.* Proc. *398* (1997), p. 793.

21 K. Batchelor *et al.*, in *Proc. of the 2nd European Particle Accelerator Conf.,* (1990), p. 541.

22 D.T. Palmer *et al.*, in *Proc. of the 1995 Particle Accelerator Conf.* (1995), p. 982. In this reference it is pointed out that the dipole emittance term has been suppressed by an order of magnitude to the level of 0.1 μm, implying that in the unsymmetrized case the dipole emittance term would be 1 μm. See also B. Dwersteg *et al.*, "rf gun design for the TESLA VUV free electron laser," *Nucl. Instrum. and Meth. A* 393 (1997) 93.

23 E.L. Ginzton, *Microwave Measurements*, McGraw-Hill (1957), p. 295.

24 X.-J. Wang *et al*., "Design studies for the LCLS 120 Hz rf gun," Informal Report BNL-67922 (Dec. 2000).

25 M. Uesaka (U. Tokyo) and M. Kando (JAERI Advanced Photon Research Center), private communication (11/00).

26 J. Schmerge, "120 Hz RF gun operation," draft of internal SLAC technical report (6/00).

27 H. Braun *et al*., "Results from the CLIC Test Facility," in *Proc. of the 5th European Particle Accelerator Conf*., (1996), p. 44.

28 T. Srinivasan-Rao *et al*., *J. Appl. Phys*. 69 (1991) 3291.

29 P. Davis *et al*., in *Proc. of the 1993 Particle Accelerator Conf*., p. 2976.

30 E. Chevallay *et al*., *Nucl. Instrum. and Meth. A* 340 (1994) 146.

31 G. Mulhollan, "Common Sense Copper and RF Guns," LCLS-TN-99-9 (July 1999).

32 D. Reis, Ph.D. Thesis, Univ. Rochester, Dept. of Physics and Astronomy, June 1999, UR-1573, pp. 130-131.

33 D. Reis *et al*., *Nucl. Instrum. and Meth. A* 429 (1999) 341.

34 D.T. Palmer, SLAC, private communication (1997).

35 X.-J. Wang et al., "FEL technologies R&D and SASE gain enhancement observation at the BNL ATF," in *Proc. of the 2000 European Particle Accelerator Conf*., p. 779.

36 The gain per pass in Ti:sapphire amplifiers is sufficient to get from 1 nJ to a few mJ in eight (8) passes. For example, see S. Backus *et al.*, *Opt. Lett.* 20 (1995) 2000.

35-1 J.A. Hoffnagle and C.M. Jefferson, Appl. Opt. 39 (2000) 5488.

37 P. Maine *et al.*, *IEEE J. Quantum Electron.* QE-24 (1988) 398.

38 A.M. Weiner *et al.*, *J. Opt. Soc. B* 5 (1988) 1563.

39 A.M. Weiner *et al.*, *Opt. Lett.* 15 (1990) 326; A.M. Weiner, *Rev. Sci. Instrum.* 71 (2000) 1929.

40 *ShapeShifter* spatial light modulator, Meadowlark Optics, Frederick, CO.

41 B.M. Van Wonterghem *et al.*, *Proc. of the Conference on Laser Coherence Control*, in *SPIE 1870* (1993), p. 64.

42 J.A. Hoffnagle and C.M. Jefferson, *Appl. Opt*. 39 (2000) 5488.

43 R.S. Craxton, *Opt. Commun.* 34 (1980) 474.

44 For ultrafast laser pulses, the effects of group velocity walkoff and nonlinear phase effects must be considered when designing the conversion stage.

45 D.A. Reis, Ph.D. Thesis, Univ. Rochester, Dept. of Physics and Astronomy, June 1999, UR-1573, pp. 23 and 131.

46 P. Davis et al., *Proc. 1993 Particle Accelerator Conf*., p. 2976.

47 H.-S. Albrecht *et al.*, *Appl. Opt*. 32 (1993) 6659.

48 D.J. Kane and R. Trebino, *Opt. Lett*. 18 (1993) 823.

49 M.J.W. Rodwell *et al.*, *Opt. Lett.* 11 (1986) 638; and M.J.W. Rodwell *et al.*, *IEEE J. Quantum Electronics* 25 (1989) 817; also T. Kotseroglou *et al.*, *Nucl. Instrum. and Meth.* A 383 (1996) 309.

50 M.J. Fitch *et al.*, "Electro-optic measurement of the wake fields of 16 MeV electron bunches," UR-1585/FERMILAB-TM-2096 (1999).

[51] I. Wilke *et al.*, "Single-Shot Electron-Beam Bunch Length Measurements," Phys. Rev. Lett. 88 (2002) 124801.